

MeCP2 Governs maternal hyperandrogenism-induced cortical defects and behavioral alterations via noncanonical AR-dependent regulation of Mef2c

Received: 23 May 2025

Accepted: 27 April 2026

Published online: 13 May 2026

 Check for updates

Yu-Meng Wang^{1,2,7}✉, Yanyan Jia^{3,7}✉, Yu Wu^{4,7}, Qiaohang Zhao⁵, Yumeng Guo⁶, Li Zhang¹✉, Min Jin⁵✉ & Yufang Zheng²✉

Elevated prenatal androgen levels have been associated with an increased incidence of several neurodevelopmental conditions in offspring. However, the underlying mechanisms remain poorly understood. Here we showed that elevated prenatal androgens, modeled via aromatase inhibition in mice, disrupt cortical development and behavior in male offspring by activating androgen receptors (AR). AR interacts with MeCP2 to upregulate the transcription factor MEF2C, bypassing standard androgen response elements. Knocking down *Mecp2* or *Mef2c*, or blocking AR, reversed these effects. *Mecp2* duplication alone also upregulated MEF2C, driving similar neurogenesis and behavioral changes that were reversed by AR blockade. This reveals a MeCP2-mediated, non-canonical pathway by which androgens may contribute to male-biased neurodevelopmental conditions.

Many neurodevelopmental conditions, such as autism, intellectual disability, and developmental language conditions, have long been recognized to exhibit a distinct sex bias in their prevalence ratios^{1–3}. Autism has demonstrated a higher prevalence among males worldwide, with a male-to-female ratio ranging from 4:1 to 6:1^{4,5}. Although a recent epidemiological research indicates a gradual decline in this sex ratio over the past two decades, the phenotypes of autism still manifest more prominently in males than females^{6,7}. The involvement of sex chromosomes and hormonal factors in the sex-biased prevalence of autism has been postulated⁸. Indeed, emerging evidence underscores the significance of steroid hormones as critical endocrine modulators in the pathogenesis of autism, consistent with the fetal

testosterone/prenatal sex steroid theory proposed by Simon Baron-Cohen^{9,10}. Research based on the Danish Historical Birth Cohort and the Danish Psychiatric Center Registry have unveiled that the levels of steroid hormones, such as progesterone and testosterone, were elevated in the amniotic fluid of males diagnosed with autism later¹¹. An interesting correlation was also observed in the studies on polycystic ovary syndrome (PCOS), an endocrine disorder characterized by hyperandrogenism in reproductive-aged females, as there is an increased risk of autism in offspring from PCOS mothers^{12–15}. In addition, several studies have unveiled a link between elevated prenatal androgen levels and notable alterations in brain morphology, including increased gray matter volume across distinct brain regions^{16–18},

¹Department of Cardiology, Institute for Developmental and Regenerative Cardiovascular Medicine, Xinhua Hospital, Shanghai Jiao Tong University School of Medicine, Shanghai, China. ²Obstetrics and Gynecology Hospital, The institute of Obstetrics and Gynecology, Shanghai key lab of reproduction and development, Shanghai key lab of female reproductive endocrine related diseases, Fudan University, Shanghai, China. ³ENT Institute and Otorhinolaryngology Department of Eye & ENT Hospital, State Key Laboratory of Medical Neurobiology and MOE Frontiers Center for Brain Science, Fudan University, Shanghai, China. ⁴Eye Institute and Department of Ophthalmology, Eye & ENT Hospital, Fudan University, Shanghai, China. ⁵Department of Reproductive Medicine, the Second Affiliated Hospital, Medical School, Zhejiang University, Hangzhou, Zhejiang, China. ⁶Department of Digestive Diseases, Huashan Hospital, Fudan University, Shanghai, China. ⁷These authors contributed equally: Yu-Meng Wang, Yanyan Jia, Yu Wu. ✉e-mail: yumeng1229@126.com; li.zhang@shsmu.edu.cn; min_jin@zju.edu.cn; zhengyf@fudan.edu.cn

suggesting a potential association between hyperandrogen exposure and abnormal brain development. However, the underlying mechanisms linking maternal hyperandrogenism to an elevated risk of autism in offspring remain poorly understood.

Precise control of neural stem cell (NSC) fate is indispensable for normal brain development and function. Abnormal regulation of neurogenesis often associated with neurodevelopmental conditions such as autism, attention deficit hyperactivity disorder (ADHD), and intellectual disability¹⁹. Previous studies utilizing human NSCs (hNSCs) has demonstrated that dihydrotestosterone (DHT) treatment on hNSCs can significantly alter gene expression^{20,21}. In addition, DHT exposure can enhance the proliferation of neural progenitor cells (NPCs) and promote the expansion of the neurogenic pool in human brain organoids²². Motivated by these observations, our study aims to examine whether maternal hyperandrogenism disrupts fetal brain development and to elucidate the underlying mechanisms.

In this study, we used a prenatal hyperandrogenism model established by aromatase inhibition, which elevates androgen levels through blockade of testosterone conversion to estradiol. We found that the cortical neurogenesis and behavioral alterations was observed in the offspring from hyperandrogenic mothers, especially in male offspring, and these effects could be prevented by administration of an androgen receptor (AR) antagonist. The effect of androgen on cortical neurogenesis is mediated through the collaborating effect of AR and Methyl-CpG Binding Protein 2 (MeCP2) on Myocyte Enhancer Factor 2C (MEF2C). Notably, AR and MeCP2 form a transcriptional activator complex and bind to the MeCP2 binding site instead of the canonical AR binding site to upregulate MEF2C expression and promote cortical neurogenesis. Moreover, MeCP2 duplication upregulated MEF2C expression and enhanced cortical neurogenesis in male offspring without prenatal hyperandrogen exposure. These effects in male offspring carrying the MeCP2 duplication were normalized by either knocking down *Mef2c* or blocking AR during gestation. Blocking AR during gestation also ameliorated behavioral alterations in male offspring carrying the MeCP2 duplication. Taken together, our findings reveal a previously unidentified mechanism mediated by MeCP2 upon androgen activation, through which maternal hyperandrogenism impairs fetal cortical development in male offspring and is linked to behavioral alterations.

Results

Maternal hyperandrogenism promotes cortical neurogenesis in offspring

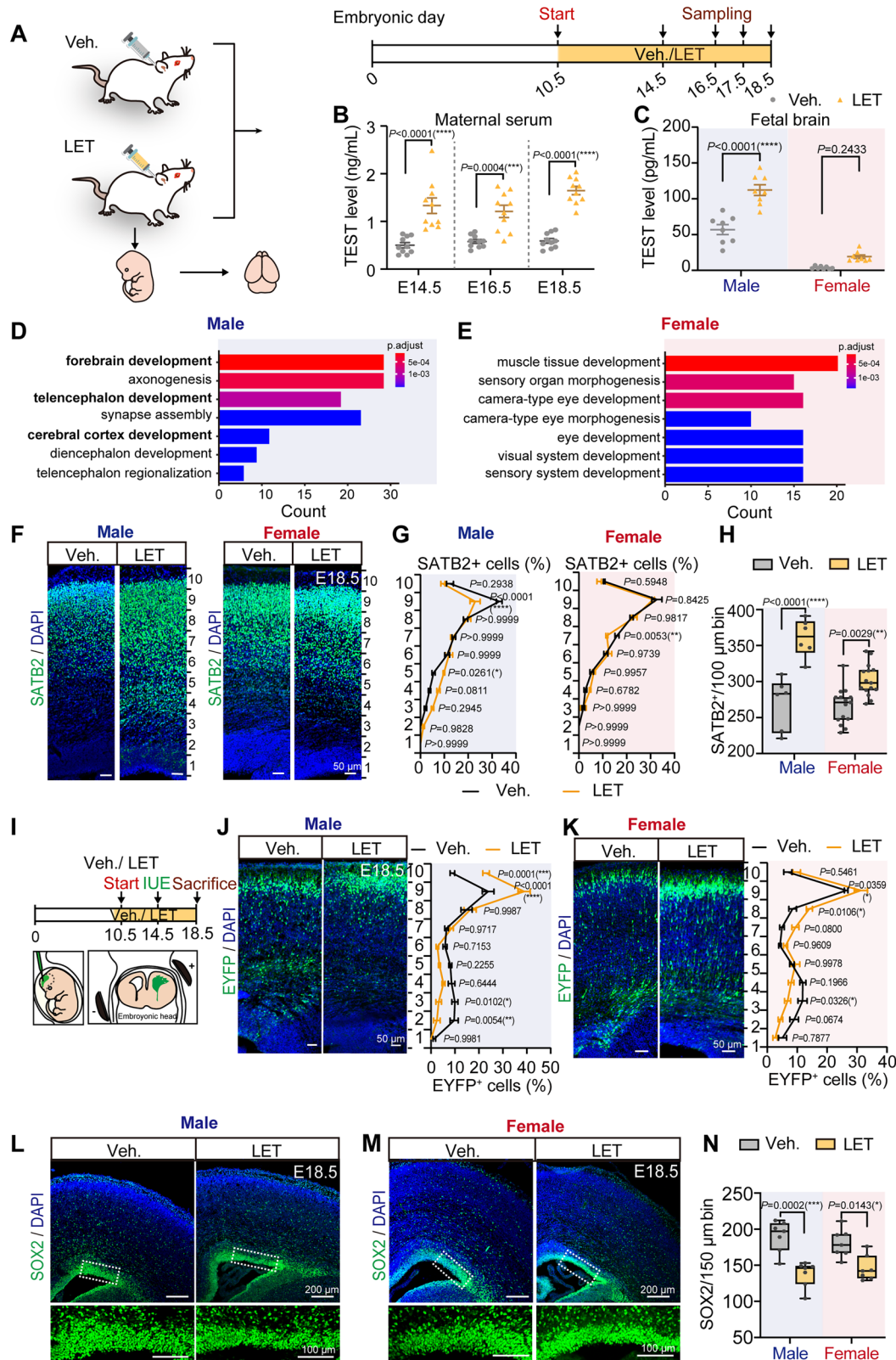
To investigate the effects of elevated prenatal androgen exposure on fetal brain development, we established a hyperandrogenic mouse model (Fig. 1A) through aromatase inhibition by administering a low dose of letrozole to pregnant mice at embryonic day 10.5 (E10.5), as previously described²³. Consistent with its effect as an aromatase inhibitor, letrozole treatment significantly increased testosterone levels in maternal serum (Fig. 1B, $N=10$ dams; partial $\eta^2=0.67$), fetal amniotic fluid (Figure S1A, male: $N=12$ from 5 dams at E14.5, $N=8$ from 5 dams at E17.5, partial $\eta^2=0.48$; female: $N=9$ from 5 dams, partial $\eta^2=0.65$), and in fetal brains (Fig. 1C, $N=8$ from 3 dams; partial $\eta^2=0.62$ for the main effect of treatment), without affecting estradiol levels in maternal serum (Supplementary Fig. S1B) and in fetal brains (Supplementary Fig. S1C). Male and female offspring exhibited increased anogenital distance, confirming effective androgen exposure (Supplementary Fig. S1D, E), while overall litter size and body weight remained unchanged (Supplementary Fig. S1F–I). To assess the potential influence of prenatal androgen exposure on labor and delivery outcomes, we analyzed key obstetric measures in vehicle-treated (Veh.) and letrozole-treated (LET) dams. Gestational length, litter size at birth, and the rates of dystocia and stillbirth were comparable between the two groups (Supplementary Table S1). These findings suggest that prenatal letrozole administration does not affect the efficiency of parturition under the present experimental conditions.

Using our prenatal hyperandrogenic mouse model, we first performed RNA sequencing (RNA-seq) on E17.5 cerebral cortices of offspring. In male offspring, differentially expressed genes (DEGs) were significantly enriched in biological processes related to forebrain and cerebral cortex development (Fig. 1D). In female offspring, however, DEGs were primarily associated with muscle tissue and eye development, with no significant enrichment in neural developmental pathways (Fig. 1E). These results suggest that prenatal androgen exposure affects brain development in a sex-dependent manner.

To further investigate the impact of maternal hyperandrogenism on cortical organization, we conducted immunohistochemical analyses using well-established cortical layer markers: SATB2 (layers II–IV), TBRI (layer VI), and CTIP2 (layers V–VI)²⁴. In male offspring exposed to hyperandrogenism, we observed striking alterations in the expression patterns and positioning of these markers. Specifically, SATB2⁺ neurons were produced prematurely as early as E13.5 (Supplementary Fig. S2A) and exhibited a broader and more dispersed distribution at E16.5 (Supplementary Fig. S2B) and E18.5 (Fig. 1F, G), accompanied by a significant increase in the number of SATB2⁺ neurons (Fig. 1H $N=8$ male from 6 dams, Cohen's $d=2.89$ at E18.5; and Supplementary Fig. S2C, $N=6$ male from 6 dams, Cohen's $d=2.88$ at E16.5). Furthermore, the number of CTIP2⁺ and TBRI⁺ neurons was increased, and their positioning was shifted downward, leading to a less organized laminar structure (Supplementary Fig. S2D–I). In female offspring, the effects were notably milder. A modest increase in SATB2⁺ neurons was observed at E18.5 (Fig. 1H, $N=15$ female from 6 dams, Cohen's $d=1.57$), but no significant change was detected at E16.5 (Supplementary Fig. S2C), and the number of CTIP2⁺ and TBRI⁺ neurons remained largely unchanged (Supplementary Fig. S2F, I), although their positioning was slightly altered compared to controls (Supplementary Fig. S2D, E, G, H). Importantly, cortical width, length, and thickness were not significantly affected in either sex (Supplementary Fig. S2J–M). The brain wet weight and total volume were also not significantly affected in either sex (Supplementary Fig. S2N, O). Collectively, these findings demonstrate that prenatal hyperandrogen exposure disrupts cortical neurogenesis and laminar organization, with male offspring exhibiting more pronounced abnormalities.

To further assess the impact of maternal hyperandrogenism on neurogenesis, we performed in utero electroporation (IUE) in embryos from hyperandrogenic mothers. EYFP-expressing constructs were electroporated into the embryonic cerebral cortex at E14.5 to label a subset of neural stem/progenitor cells (NSCs/NPCs) that differentiate into immature neurons and migrate radially toward the cortical plate (CP) to form mature neurons (Fig. 1I). The differentiation and migration of labeled NSCs/NPCs were examined at E18.5. In male offspring exposed to hyperandrogenism, we observed a significant increase in the number of EYFP⁺ cells that migrated into the upper CP compared to controls (Fig. 1J; $N=6$ from 5 dams). In female offspring, a similar but less pronounced increase was noted (Fig. 1K; $N=6$ from 5 dams). These findings from the IUE experiments are consistent with our data from the prenatal hyperandrogen exposure model.

To further elucidate the mechanisms responsible for altered neurogenesis, we quantified SOX2⁺ early NSCs/NPCs and TBR2⁺ intermediate progenitor cells (IPs) in the E18.5 cortex. Male offspring exposed to hyperandrogenism exhibited a significant reduction in SOX2⁺ NSCs/NPCs (Fig. 1L, $N=13$ from 5 dams; Cohen's $d=2.87$) and an increase in TBR2⁺ IPs compared to controls (Supplementary Fig. S3A, B, $N=13$ from 5 dams; Cohen's $d=2.02$). In females, only a mild decrease in SOX2⁺ cells (Fig. 1M, N) was observed without a significant change in TBR2⁺ IPs (Supplementary Fig. S3A, B). Furthermore, a significant reduction in EAAT1⁺ astrocytes was observed in postnatal male offspring but not in females (Supplementary Fig. S3C, D). Taken together, these results suggest that maternal hyperandrogenism promotes neurogenesis in male offspring by affecting the cell fate of NSCs/NPCs during cortical development. Again, the effect is much milder in female offspring.



Maternal hyperandrogenism promotes social and non-social behavior in offspring, particularly in male offspring

We next evaluated social and non-social behaviors in both male and female offspring of hyperandrogenic mothers. To minimize potential confounding effects of postnatal maternal care, all newborn pups were cross-fostered to vehicle-treated control dams immediately after birth (Fig. 2A). To assess social interactions, adult

offspring underwent the three-chamber social interaction test. During the sociability phase, mice were given the choice to interact with either an unfamiliar mouse or an empty cage (Fig. 2B; $N=17$ from 9 dams). Male offspring exposed to prenatal hyperandrogenism exhibited a significantly reduction in interaction time with an unfamiliar mouse compared to vehicle-treated controls (Fig. 2C; Cohen’s $d=1.98$). In contrast, no such reduction in interaction time

Fig. 1 | Maternal hyperandrogen promotes cortical neurogenesis in offspring.

A Schematic of the design and letrozole treatment regimen. Pregnant mice were administered daily subcutaneous injections of letrozole or vehicle from E10.5 to E17.5. **B** Serum testosterone levels in pregnant dams were measured at E14.5, E16.5 and E18.5 ($N = 10$ per group). **C** Fetal brain testosterone levels were assessed at E18.5 ($N = 8$ per group from 3 dams). **D, E** Bulk RNA-seq was performed on E17.5 cerebral cortices from male and female offspring ($N = 3$ per group, each from a separate dam). Differentially expressed genes were identified using thresholds of $P < 0.05$ and $|\log_2(\text{fold change})| > 0.3$, followed by ontology enrichment analysis. **F–H** SATB2⁺ neurons (green) were immunolabelled in E18.5 cortices. The cortex was divided into 10 equal-width bins (100 μm each) from ventricular to pial surface to quantify distribution. Nuclei were counterstained with DAPI (blue). Representative images (**F**) and bin-wise distribution of SATB2⁺ (**G**) cells are shown ($N = 6$ per sex per group

from 6 dams). The number of SATB2⁺ cells is shown in (**H**) ($N = 6$ males, 15 females from 6 dams). Scale bar, 50 μm . **I** Schematic of *in utero* electroporation (IUE) with an EYFP plasmid at E14.5 during letrozole treatment. **J, K** EYFP⁺ cell distribution was analyzed in male (**J**) and female (**K**) cortices at E18.5 ($N = 6$ per sex from 5 dams per group). Confocal images and bin-wise quantification are shown. Scale bars, 50 μm . **L–N** SOX2⁺ progenitors were visualized and quantified in E18.5 cortices ($N = 13$ per sex per group from 5 dams; Scale bars: 200 μm). Counts were performed per 150 μm bin. Insets show higher-magnification views (Scale bars: 100 μm). Data are expressed as the means \pm SEM. Box plots show the median (center line), 25th–75th percentiles (box limits), and whiskers indicate the minimum and maximum values. Statistical analyses were performed with two-tailed unpaired Student's *t* test (**B, C**) or two-way ANOVA test followed by Sidak *post-hoc* test (**G, H, J, K** and **N**). Exact *P*-values are indicated. * $P < 0.05$; ** $P < 0.01$; *** $P < 0.001$; **** $P < 0.0001$.

was observed in female offspring (Fig. 2C; Cohen's $d = 0.16$). In the subsequent social novelty phase, a novel mouse was introduced into the previously empty cage (Fig. 2D). Male offspring from hyperandrogenic mothers showed a significantly lower social novelty index relative to controls (Fig. 2E; Cohen's $d = 2.45$), whereas female offspring displayed no significant differences (Fig. 2E; Cohen's $d = 0.18$). These findings suggest that maternal hyperandrogenism reduces social novelty selectively in male offspring.

Given that comorbid anxiety symptoms and motor abnormalities are often associated with autism, we next evaluated locomotor activity and anxiety-like behavior using the open field (OF, Fig. 2F–J) and elevated plus maze (EPM, Fig. 2K, L) tests ($N = 19$ from 9 dams). Both male and female offspring exhibited normal locomotor activity, as evidenced by comparable total distance traveled and movement time in the OF test (Fig. 2G, H). However, male offspring from hyperandrogenic mothers displayed elevated anxiety-like behavior, characterized by diminished central zone preference in the OF test (Fig. 2I, J; OF center ratio, Cohen's $d = 1.760$), and distance traveled in the open arms in the EPM test (Fig. 2K, L; Cohen's $d = 1.91$). In contrast, female offspring showed no significant alterations in anxiety-like behavior (Fig. 2I–L).

We further assessed non-social interest-related and perseverative behaviors using the marble-burying test, a commonly used behavioral paradigm in genetically modified mouse models^{25–27}. Male offspring from hyperandrogenic mothers buried significantly more marbles compared to controls (Fig. 2M; $N = 19$ from 9 dams; Cohen's $d = 2.41$). No significant difference in marble-burying behavior was observed in female offspring (Fig. 2M).

Collectively, our results indicate that prenatal hyperandrogenism induces prominent behavioral abnormalities in male offspring, including reduced social novelty, increased non-social perseverative behaviors, and heightened anxiety, whereas female offspring are largely unaffected.

AR is essential for cortical neurogenesis in male offspring of hyperandrogenic mothers

We next sought to investigate the molecular mechanisms underlying the effects of maternal hyperandrogenism on fetal cortical development. As a key downstream effector of androgen signaling, the androgen receptor (AR) binds to androgens, translocates to the nucleus, and functions as a transcription factor²⁸. We therefore examined AR expression in the embryonic cortex of both male and female offspring. At E14.5, significantly stronger AR expression was observed in the cortex of male offspring as compared to female offspring (Fig. 3A; $N = 6$ from 6 dams; Cohen's $d = 3.03$). In female offspring, AR expression was scarcely detectable (Fig. 3A, C). Furthermore, a significant upregulation of AR protein levels was observed in the cerebral cortex of male offspring from hyperandrogenic mothers compared to controls (Fig. 3B and Supplementary Fig. S4A, B; $N = 7$ from 6 dams; Cohen's $d = 3.88$), whereas no obvious change was detected in female offspring (Fig. 3C). Notably, the mRNA

expression of *Ar* in male offspring remained unchanged between groups (Supplementary Fig. S4C).

The increased AR protein levels in male offspring imply that the androgen/AR signaling axis is more active compared to that in females. We thus focused our subsequent analyses on male offspring. To determine the role of AR signaling, we performed AR blockade by injecting flutamide, an AR antagonist, into the lateral ventricle at E14.5 in the maternal hyperandrogenism model (Fig. 3D). Analysis at E18.5 revealed that flutamide treatment effectively rescued the enhanced neurogenesis phenotype induced by letrozole ($N = 8$ from 6 dams). Specifically, the number of SATB2⁺ neurons (LET + Veh. vs LET + FT, Cohen's $d = 2.26$) and SOX2⁺ NSCs/NPCs (LET + Veh. vs LET + FT, Cohen's $d = 2.13$) was restored to levels comparable to controls (Fig. 3E, F).

To further confirm the role of AR, we also performed IUE to introduce EYFP together with either scramble shRNA or AR-targeting shRNA into the embryonic cortex. The AR shRNA sequence was adopted from previous studies²⁹. Western blot analysis confirmed efficient AR knockdown (Supplementary Fig. S7A). Consistent with pharmacological blockade, AR knockdown rescued the neurogenesis phenotype, as indicated by a higher proportion of EYFP⁺ cells retained in the VZ/SVZ and IZ, and a reduced fraction migrating into the upper CP (Fig. 3G; $N = 6$ from 4 dams).

We next validated these findings *in vitro* using primary NPCs isolated from E14.5 mouse cortices. Cells were treated with vehicle (DMSO), dihydrotestosterone (DHT, 10 nM) alone, or DHT in combination with flutamide (0.4 μM) for 72 h. DHT was used to achieve selective and direct activation of AR. Unlike testosterone, DHT is not subject to aromatization into estrogens, which facilitates the examination of AR-dependent effects without confounding influences from estrogen receptor signaling or other steroidogenic conversions. DHT treatment significantly increased AR expression and promoted its nuclear translocation (Supplementary Fig. S5A), while flutamide did not alter AR protein levels (Supplementary Fig. S5B). DHT treatment led to a significant increase in the neuronal marker MAP2, accompanied by a decrease in the NSC/NPC marker Nestin and the astrocyte marker GFAP (Supplementary Fig. S5B–F). Immunofluorescence staining corroborated these findings (Fig. 3H; $N = 4$), showing an increased number of MAP2⁺ and a reduced number of GFAP⁺ and Nestin⁺ cells following DHT treatment. Co-treatment with flutamide effectively blocked these DHT-induced changes (Supplementary Fig. S5B–F and Fig. 3H).

To further assess whether these effects are conserved across species, we next examined androgen signaling in a human stem cell-derived neural differentiation model. H1 human embryonic stem cells were first differentiated into neural stem cells (NSCs) and subsequently induced to neurons in the presence of DHT (10 nM), with or without co-treatment with flutamide (0.4 μM) for 7 days. DHT treatment increased nuclear AR localization and overall AR protein levels, whereas flutamide co-treatment did not alter AR expression (Supplementary Fig. S6A, B). During neuronal differentiation, DHT increased

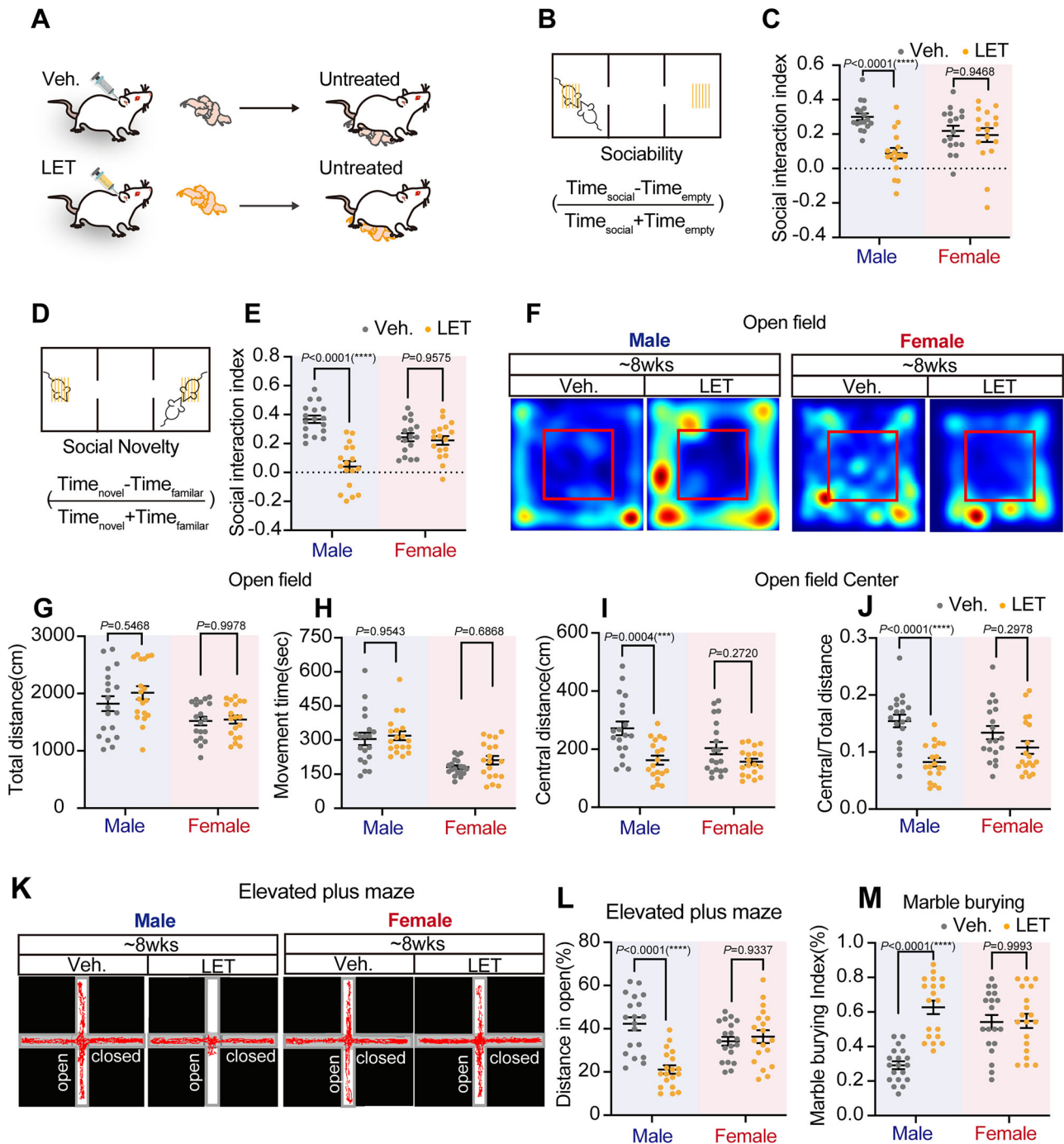


Fig. 2 | Male offspring of hyperandrogenic mothers exhibit autism-like behaviors. **A** Schematic illustration of the cross-fostering strategy used to control for potential effects of altered maternal behavior. Newborn pups from vehicle (Veh.)- or letrozole (LET)-treated dams were closely monitored around the expected time of delivery and immediately transferred at birth to untreated surrogate dams, which raised the pups until weaning. **B** Schematics of the three-chamber social interaction test. **C** Social interaction index ($N = 17$ from 9 dams, for each group) in control and letrozole-treated mice. **D** Schematics of the three-chamber social novelty test. **E** Social novelty index ($N = 17$ from 9 dams, for each group). **F** Representative heatmaps of locomotion patterns in the open field test for vehicle-

and letrozole-treated males (left) and females (right). **G–J** Quantification of total distance (**G**), movement time (**H**), center/total distance (**I**) and center/total distance ratio (**J**). $N = 19$ from 9 dams per group. **K** Representative tracking traces in the elevated plus maze (EPM) for male offspring. **L** Distance traveled in the open arms of the EPM. $N = 19$ from 9 dams for each group. **M** Marble burying index, calculated as the number of buried marbles divided by the total. $N = 19$ per sex from 9 dam per group. All data are expressed as the means \pm SEM. Exact P -values are indicated. Statistical analyses: two-way ANOVA test followed by Sidak *post-hoc* test. * $P < 0.05$; ** $P < 0.01$; *** $P < 0.001$; **** $P < 0.0001$.

the expression of the neuronal marker MAP2 and reduced the expression of the NSC marker Nestin; which were also largely reversed by co-treatment with flutamide (Supplementary Fig. S6C–F; $N = 5$).

Furthermore, lentivirus-mediated AR knockdown reversed the effects of DHT on NPC differentiation, similar to the effects observed

with flutamide (Fig. 3I and Supplementary Fig. S7A–D, $N = 5$), supporting the critical role of AR signaling. To determine whether AR activation alone could mimic the effects of hyperandrogen, we over-expressed a constitutively active form of AR (AR-V7)³⁰ in mouse NPCs. Western blot confirmed successful AR overexpression (Supplementary

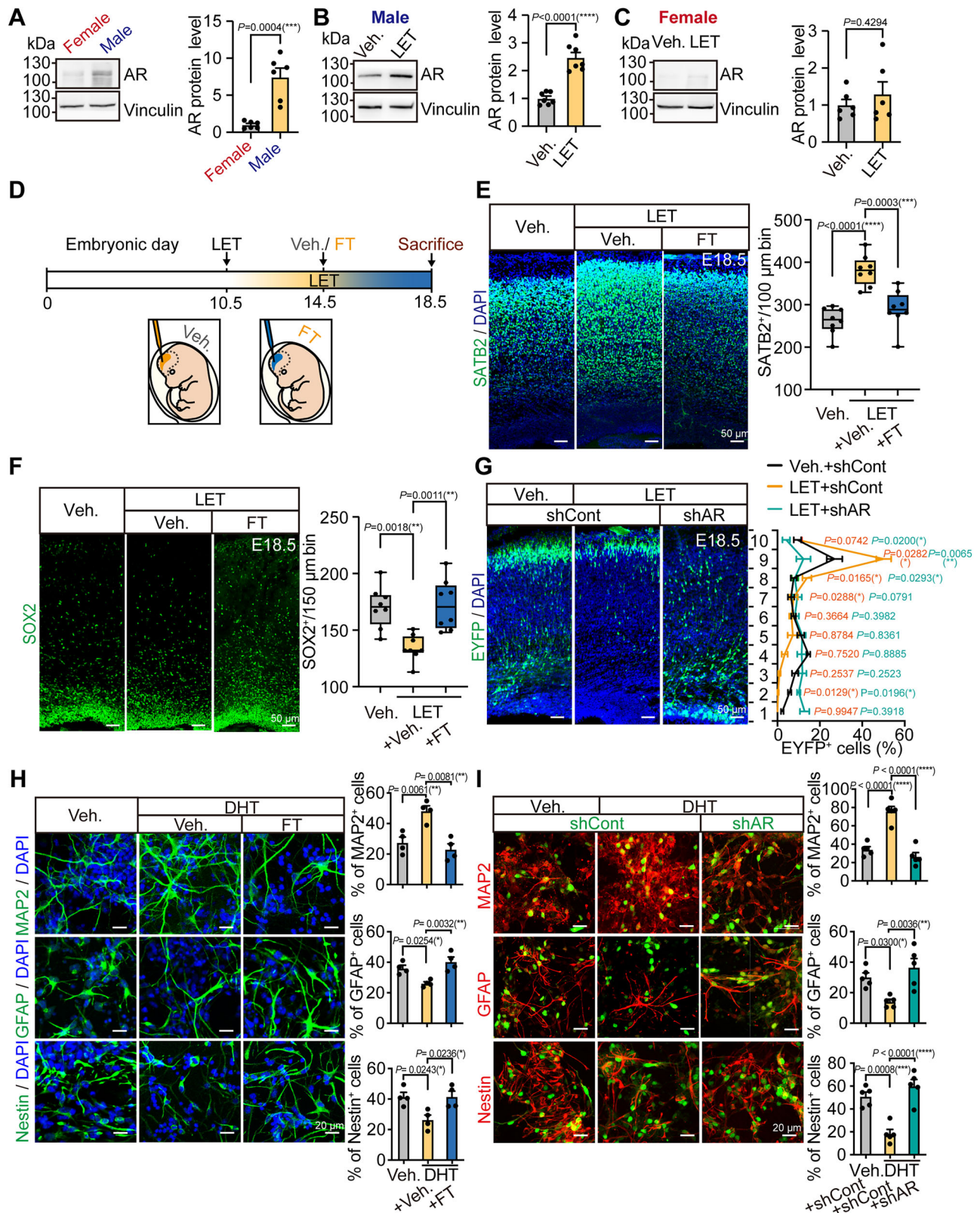


Fig. S7F). Notably, AR-V7 overexpression recapitulated the effects of DHT, promoting neuronal differentiation and inhibiting glial and progenitor markers, as demonstrated by both immunofluorescence staining (Supplementary Fig. S7E) and western blot analyses (Supplementary Fig. S7F-I).

To determine whether AR signaling contributes to the behavioral alterations induced by prenatal hyperandrogenism, we performed

additional behavioral analyses comparing offspring treated with letrozole alone (LET + Veh.) and those receiving additional AR blockade (LET + FT). Again, behavioral assessments, including three-chamber social interaction, open field, marble burying, and elevated plus maze tests, were performed (Supplementary Fig. S8). In the three-chamber social interaction assay (Supplementary Fig. S8A-D; $N=16$ from 10 dams), AR blockade significantly improved both sociability

Fig. 3 | Blocking AR can reverse the upregulated cortical neurogenesis in the male offspring of hyperandrogenic mothers. **A–C** Western blot analysis showed AR protein levels in the cerebral cortex of E14.5 male and female offspring (**A**; $N = 6$ per sex from 6 dams), with quantification in male (**B**; $N = 7$ from 6 dams) and female (**C**; $N = 6$ from 6 dams) embryos from vehicle- or letrozole-treated groups. **D** Schematic of flutamide (FT) administration in the maternal hyperandrogenism model, in which E14.5 embryos from vehicle- or letrozole-treated dams were injected intracerebrally with vehicle or FT (0.6 μg), and cortices were collected at E18.5. **E, F** Representative immunostaining and quantification of SATB2⁺ and SOX2⁺ cells in cortices from vehicle-, letrozole-, and letrozole + FT treated groups ($N = 8$ male offspring from 6 dams). Quantification was performed per 100 μm (SATB2) or 150 μm (SOX2) bin. Scale bars, 50 μm . **G** Confocal imaging and quantification of EYFP⁺ cell distribution across cortical layers at E18.5 in IUE experiments ($N = 6$ male

offspring from 4 dams). Scale bar, 50 μm . **H** Mouse primary NPCs were treated with vehicle, DHT (10 nM), or DHT + FT, followed by immunostaining for MAP2, GFAP, and Nestin ($N = 4$ independent cultures). Scale bar, 20 μm . Quantification of marker-positive cells are presented on the right. **I** NPCs were infected with control or shAR lentivirus (EGFP-labeled) and stained for MAP2, GFAP, and Nestin (pseudo-colored red). Quantification of marker-positive cells among EGFP⁺ populations is shown ($N = 5$ independent experiments). Scale bar, 20 μm . All data are presented as the means \pm SEM. Box plots show the median (center line), 25th–75th percentiles (box limits), and whiskers indicate the minimum and maximum values. Exact P -values are indicated. * $P < 0.05$; ** $P < 0.01$; *** $P < 0.001$; **** $P < 0.0001$. Two-way ANOVA followed by Sidak *post-hoc* test was performed for (**G**). Two-tailed unpaired Student's t test was performed for (**A–C**). One-way ANOVA followed by Tukey *post-hoc* test was performed for (**E, F** and **H, I**).

(LET + Veh. vs LET + FT, Cohen's $d = 2.01$) and social novelty (LET + Veh. vs LET + FT, Cohen's $d = 1.44$) indices in letrozole-exposed offspring, restoring social interaction performance toward control levels. In the open field test (Figure S8E–G; $N = 19$ from 10 dams), flutamide treatment did not alter total locomotor activity but significantly increased center exploration (LET + Veh. vs LET + FT, Cohen's $d = 1.97$), indicating an attenuation of anxiety-related behavior. In addition, AR inhibition markedly reduced marble-burying behavior (Supplementary Fig. S8H; $N = 2$ from 10 dams), reflecting normalization of non-social interest-related and perseverative behaviors (LET + Veh. vs LET + FT, Cohen's $d = 2.63$). Consistently, performance in the elevated plus maze (Figure S8I, J; $N = 19$ from 10 dams) showed increased exploration of open arms following AR blockade (LET + Veh. vs LET + FT, Cohen's $d = 1.70$), further supporting reduced anxiety-like behavior.

Taken together, our results provide compelling evidence that maternal hyperandrogenism promotes neurogenesis and behavioral alterations through the activation of AR signaling pathways in male offspring.

MEF2C is downstream of AR in hyperandrogen promoted neurogenesis

To identify potential AR downstream targets mediating hyperandrogenism-induced neurogenesis, we analyzed the differentially expressed genes (DEGs) from the RNA-seq data of E17.5 male cerebral cortices. By cross-referencing these DEGs with an independent RNA-seq dataset of human NSCs treated with DHT¹³, we identified 26 overlapping genes (Fig. 4A and Supplementary Fig. S9, 11 upregulated, 15 downregulated). Although substantial transcriptional divergence was observed between the in vivo mouse cortex and in vitro hNSC models (as quantified by hypergeometric testing, see Fig. 4A legend), this conserved set of genes provided a stringent, high-priority pool of candidates for subsequent functional validation. Given our findings indicating hyperandrogen enhancing neurogenesis, we examined these 26 genes using a published single-cell RNA-seq dataset tracking radial glial cells (RGCs) and their progenies during mouse cortical neurogenesis³¹. 24 out of 26 genes are presented in this dataset. Among these 24 genes, four (*Mef2c*, *Bhlhe22*, *Ndufaf8*, and *Chrcl1*) exhibited dynamic regulation during cortical neurogenesis (Fig. 4B), whereas others 20 genes remained relatively stable (Supplementary Fig. S10). qRT-PCR validation in cortical tissues confirmed these expression alterations in male offspring from hyperandrogenic mothers (Fig. 4C and Supplementary Fig. S11; $N = 4$). Notably, based on previous studies^{21,32}, *Mef2c* is the only AR-bound gene within the four dynamic regulated genes (Fig. 4D).

MEF2C has been implicated in autism and other neurodevelopmental conditions^{33–35} and was upregulated by DHT in human iPSC models derived from autistic individuals²⁰. Consistently, we observed elevated MEF2C protein expression and an increased number of MEF2C⁺ cells in the cerebral cortices of male offspring from hyperandrogenic mothers (Fig. 4E–H). Further in vitro studies confirmed that DHT significantly enhanced MEF2C expression at both mRNA and protein levels in cultured NPCs, while co-treatment with flutamide

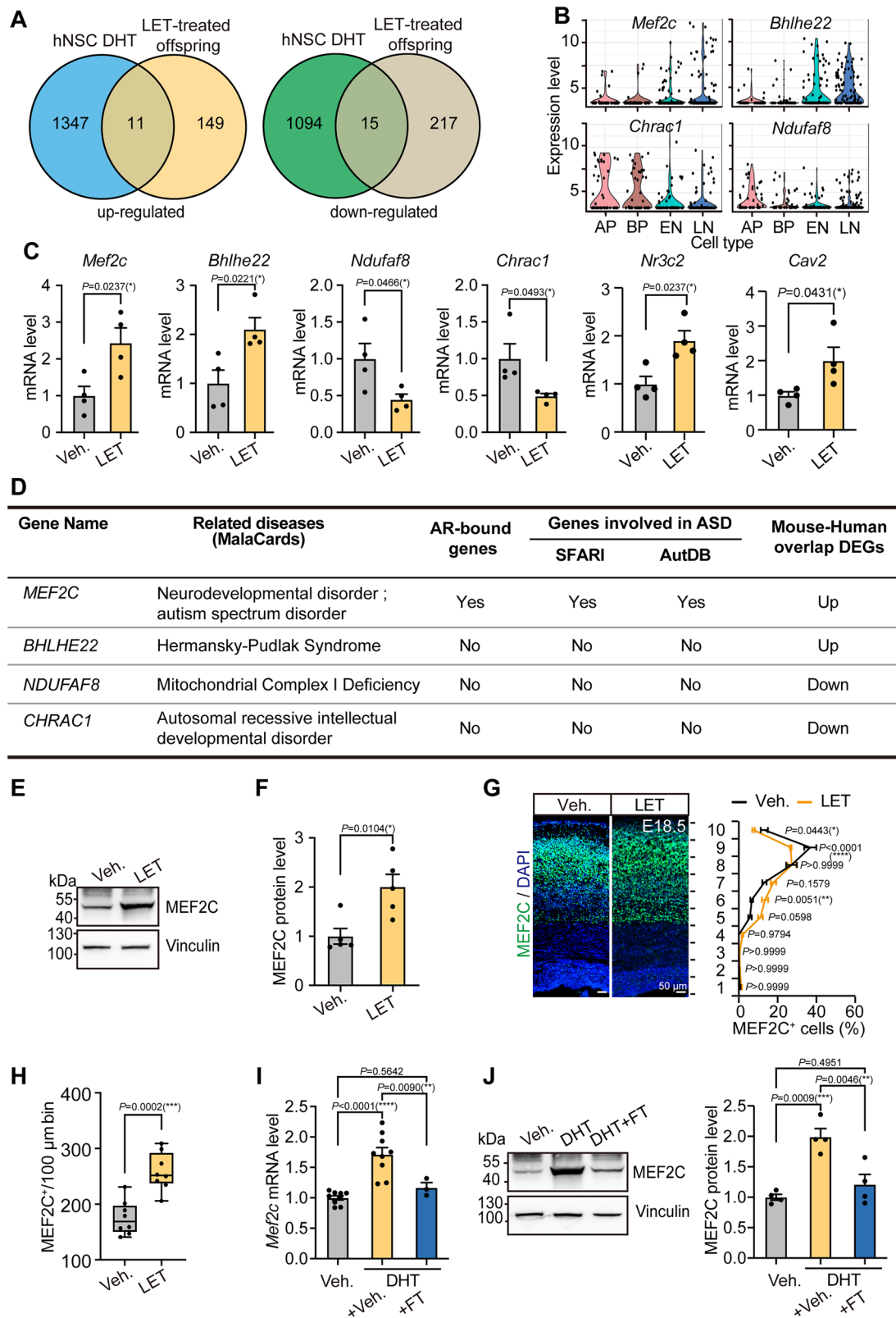
reversed these effects (Fig. 4I, J). These results collectively suggest that MEF2C acts as a critical downstream effector of hyperandrogen.

To validate the essential role of MEF2C in vivo, we performed IUE at E14.5 to introduce EYFP constructs along with either scramble shRNA or *Mef2c*-specific shRNA into the embryonic cortex of male mice from hyperandrogenic mothers (Fig. 5A). Efficient MEF2C knockdown by shRNA4 was confirmed in Neuro 2A (N2a) cells (Supplementary Fig. S12A) and primary mouse NPCs (Supplementary Fig. S12B). Analysis of cortical cell distribution after IUE revealed that knockdown of MEF2C significantly attenuated hyperandrogen-induced neurogenesis. Specifically, MEF2C knockdown resulted in an increased proportion of EYFP⁺ cells retained in the ventricular/subventricular zone (VZ/SVZ) and intermediate zone (IZ), and reduced migration into the cortical plate (CP) (Fig. 5B). Supporting these findings, lentivirus-mediated *Mef2c* knockdown in primary NPCs reversed the effects of DHT on neuronal differentiation, as demonstrated by western blot analysis (Fig. 5C–F; $N = 4$) and immunofluorescent staining (Fig. 5G; $N = 4$) for MAP2, GFAP, and Nestin. These findings support that MEF2C is critical for maternal hyperandrogenism-induced neurogenesis in male offspring.

The upregulation of Mef2c by AR is dependent on MeCP2

To investigate how AR transcriptionally regulates *Mef2c* in mice, we performed a sequence analysis of the mouse *Mef2c* locus to identify potential AR binding sites. Based on ENCODE data annotations, we identified multiple regulatory regions, including promoter and enhancers, near the transcriptional start site of the *Mef2c* gene (Fig. 6A and Supplementary Fig. S13A). Among these, one conserved AR binding site ARE (androgen response element)³² was located within enhancer E0566845 (Fig. 6A). Chromatin immunoprecipitation followed by qPCR (ChIP-qPCR) assays in N2a cells expressing AR showed enriched AR binding not only at this predicted ARE but also at the promoter-E0566843 region upon DHT stimulation (Fig. 6B–D and Supplementary Fig. S13B–F). Intriguingly, promoter-E0566843 also harbors a previously characterized MeCP2 binding site³⁶. ChIP-qPCR confirmed MeCP2 occupancy at this promoter region (Fig. 6E), but not the CpG island of the *Mef2c* gene (Fig. 6F). Importantly, AR binding was significantly enriched at the MeCP2 binding site following DHT treatment (Fig. 6G). In addition, MeCP2 unexpectedly bound to the predicted AR binding site, an interaction further enhanced by DHT (Fig. 6H).

To further investigate the cooperative role of AR and MeCP2 in regulating *Mef2c* expression, we constructed a luciferase reporter plasmid containing both AR and MeCP2 binding sites (*Mef2c*-WT). Luciferase assays in N2a cells revealed significantly enhanced reporter activity upon co-expression of AR and MeCP2 following DHT treatment, while individual expression of AR or MeCP2 resulted in only modest increases (Fig. 6I). Without DHT treatment, AR or MeCP2 alone did not enhance luciferase activity (Supplementary Fig. S13G), suggesting androgen-induced AR activation is essential is required for the upregulation of *Mef2c*. To further dissect the contributions of the individual binding sites, we generated three



truncated mutants of the *Mef2c* promoter (*Mef2c*-ΔAR, *Mef2c*-ΔMe, and *Mef2c*-ΔARΔMe) (Fig. 6J). N2a cells were transfected with either *Mef2c*-WT or different deletion mutant and treated with DHT. We observe that the co-transfection of MeCP2 and AR significantly increased luciferase activity of *Mef2c*-WT, and revealed that deletion of the MeCP2 binding site (*Mef2c*-ΔMe), but not the ARE (*Mef2c*-ΔAR), abrogated AR/MeCP2-mediated upregulation (Fig. 6J). These

findings indicate that androgen-activated AR upregulation on *Mef2c* is depends on MeCP2.

Given the transcriptional cooperation observed, we then investigated whether AR and MeCP2 can directly interact. Co-immunoprecipitation analysis confirmed physical interaction between AR and MeCP2 in the presence of DHT (Fig. 6K, L), while no interaction was detected without DHT (Supplementary Fig. S13H, I).

Fig. 4 | MEF2C was downstream of AR in hyperandrogen promoted neurogenesis in mouse cortex. **A** Venn diagrams show the overlap between genes differentially expressed in DHT-treated hNSCs²¹ and genes altered in letrozole-treated embryonic cortex. Human genes were converted to mouse orthologs (GRCh38.p13 to GRCm39). Overlap significance was assessed against 16,096 conserved one-to-one orthologs using two-tailed hypergeometric tests. No enrichment was observed (up-regulated: $P = 0.62$, down-regulated: $P = 0.85$). **B** Violin plots show dynamic expression of four genes across cell populations from a single-cell RNA-seq dataset of embryonic mouse cortex⁶⁶. AP: Apical progenitors/RGCs; BP: daughter basal progenitors/IPCs; EN: early neurons; LN: late neurons. **C** Validation of 6 genes by qRT-PCR in E17.5 cortices ($N = 4$ males from 4 dams). **D** Functional annotation of the four genes, including autism associations (from SFARI & AutDB databases) and AR binding based on published ChIP-seq datasets^{21,39}. Related disease information is

from the MalaCards-human disease database. **E, F** Western blot analysis of MEF2C protein levels in E17.5 cortices from vehicle- and letrozole-treated embryos ($N = 5$ males from 4 dams), normalized to vehicle controls. **G** Immunofluorescence and quantification of MEF2C⁺ cells at E18.5 across 10 cortical zones ($N = 6$ males from 6 dams). **H** Quantification of MEF2C⁺ cells per 100 μm^2 bin ($N = 8$ males from 6 dams). Scale bars, 50 μm . **I, J** Mouse NPCs treated with vehicle, DHT (10 nM), or DHT plus flutamide (FT). **I** *Mef2c* mRNA levels were measured by qRT-PCR ($N = 9$ for vehicle and vehicle + DHT, $N = 3$ for DHT + FT); and **J** MEF2C protein levels were detected by western blot ($N = 4$). Vinculin was used as the loading control. All data were expressed as means \pm SEM. Exact P values are indicated. * $P < 0.05$; ** $P < 0.01$; *** $P < 0.001$; **** $P < 0.0001$. Two-tailed unpaired Student's t test was performed for (**C, F** and **H**). Two-way ANOVA tests followed by Sidak *post-hoc* test was performed for (**G**). One-way ANOVA followed by Tukey *post-hoc* test was performed for (**I, J**).

Furthermore, flutamide treatment effectively blocked the upregulation of luciferase activity in cells expressing the *Mef2c*- Δ AR luciferase reporter (Fig. 6M). Consistently, although co-expression of MeCP2 and AR enhanced luciferase activity in cells with the *Mef2c*- Δ AR luciferase reporter, expression of AR alone failed to activate transcription (Fig. 6N). MeCP2 knockdown (knockdown efficiencies presented in Supplementary Fig. S13J, K) did not further decrease baseline reporter activity (Fig. 6N). Given the transcriptional cooperation observed between AR and MeCP2, we next sought to confirm whether MeCP2 is essential for AR-dependent neurogenesis in vivo. To this end, we performed MeCP2 knockdown via IUE in male offspring from hyperandrogenic mothers. Importantly, knocking down MeCP2 effectively reversed the aberrant neuronal migration phenotype induced by prenatal hyperandrogenism (Fig. 6O), reinforcing MeCP2's critical role in mediating AR-dependent cortical neurogenesis. Collectively, these results strongly support a MeCP2-dependent AR activation on *Mef2c* transcription in cortical neurogenesis (Fig. 6P).

Blocking AR or downregulating *Mef2c* can rescue the enhanced cortical neurogenesis caused by MeCP2 duplication in male offspring

So far, we have found that the effect of hyperandrogen on cortical neurogenesis is mediated through the collaborating effect of AR and MeCP2 on MEF2C. Given the critical role of MeCP2 in this non-ARE regulatory pathway, we propose that overdosed MeCP2 probably could activate this pathway in male mice, even without prenatal hyperandrogen exposure.

We previously reported elevated cortical neurogenesis in the fetal brain of the MeCP2^{Tg1} autism mouse model harboring an additional human *MECP2* copy³⁷. This phenotype is very similar to the effect induced by prenatal hyperandrogen exposure. Therefore, we want to check whether MEF2C is also upregulated in these MeCP2^{Tg1} male mice. Indeed, western blot and immunofluorescent experiments on cortical tissue revealed that MEF2C expression was elevated in MeCP2^{Tg1} male cortices (Fig. 7A–C). Using IUE to deliver *Mef2c* shRNA into E14.5 MeCP2^{Tg1} embryos (Fig. 7D), we found that knocking down *Mef2c* significantly reversed the aberrant cortical neuron migration phenotype at E18.5. Specifically, more EYFP⁺ cells remained in the VZ/SVZ and IZ regions, with fewer reaching the cortical plate (Fig. 7E). In vitro analyses using primary neural progenitor cells (NPCs) isolated from MeCP2^{Tg1} mice further confirmed that *Mef2c* knockdown effectively reversed MeCP2 duplication-induced differentiation changes, as demonstrated by western blot (Fig. 7F–I) and immunostaining for MAP2 and GFAP (Fig. 7J–M). These findings support that MEF2C is downstream of MeCP2 in promoting neurogenesis in male mice.

What's more, we also evaluated whether pharmacological AR blockade could similarly rescue neurogenesis abnormalities in MeCP2^{Tg1} mice. Administration of flutamide to E14.5 MeCP2^{Tg1} embryos normalized elevated MEF2C expression at E18.5 to levels comparable to wild-type controls (Fig. 8A–C). In line with our earlier study³⁷, MeCP2^{Tg1} embryos displayed increased SATB2⁺ neurons and reduced

SOX2⁺ neural progenitors, both of which were partially rescued by flutamide treatment (Fig. 8D, E). In addition, primary NPC cultures isolated from MeCP2^{Tg1} mice were treated with DHT, resulting in enhanced neuronal differentiation. This effect was suppressed by flutamide in a dose-dependently manner (Supplementary Fig. S14A–D). Similarly, concurrent MeCP2 overexpression and DHT treatment in WT NPCs promoted neuronal differentiation, an effect that was also blocked by flutamide (Supplementary Fig. S14E–I).

Furthermore, to examine whether pharmacological blockade of AR signaling could rescue autism-like behavioral abnormalities in MeCP2^{Tg1} male mice, we administered flutamide via lateral ventricular injection at E14.5 and subsequently evaluated behaviors in adult male offspring. MeCP2^{Tg1} male mice displayed reduced social novelty and altered social interaction, increased repetitive behaviors in the marble-burying test, and heightened anxiety-like behaviors in the open field and elevated plus maze tests. Remarkably, flutamide treatment effectively ameliorated these behavioral deficits specifically in male MeCP2^{Tg1} offspring, restoring their performance to levels comparable to wild-type controls (Fig. 8F–M, $N \geq 18$ males from 10 dams). In contrast, flutamide treatment did not significantly rescue the behavioral alterations observed in female MeCP2^{Tg1} mice (Supplementary Fig. S15, $N \geq 18$ females from 10 dams).

Discussion

In this study, we investigated the association between elevated maternal androgen levels and neurodevelopment outcomes in offspring. Our results suggest that maternal hyperandrogenism affects fetal brain development and has a much stronger effect on male offspring in both cortical neurogenesis and behavior. Mechanistically, we identify MEF2C as a critical downstream effector of AR signaling in the developing cortex. Upon DHT stimulation, AR forms a complex with MeCP2 and binds to the MeCP2 binding site, rather than the canonical ARE, within the *Mef2c* regulatory region (Supplementary Fig. S16). Knockdown of either MEF2C or MeCP2 reversed the effect of maternal hyperandrogenism on cortical development. Furthermore, downregulation of MEF2C or AR in MeCP2^{Tg1} male mice counteracts the enhanced cortical neurogenesis induced by MeCP2 duplication. Together, these results delineate a MeCP2-dependent, non-ARE-mediated AR regulatory pathway and offer mechanistic insight into how maternal hyperandrogenism affects neurodevelopmental processes.

Here, we identify that MEF2C as a critical factor in hyperandrogen-promoted neurogenesis. MEF2C is highly expressed in the fetal brain in both humans and mice, especially in the cerebral cortex^{38–40}. Conditional knockout of *Mef2c* in mouse NSCs/NPCs affects neuronal differentiation, resulting in abnormal density and cell body sizes of cortical plate neurons³⁵. Consistent with its role in development, human genetic studies have identified *MEF2C* as a causative gene in neurodevelopmental disorders⁴¹. Large-scale genetic screening of ASD and intellectual disability (ID) cohorts indicates that loss-of-function variants or copy number variations affecting *MEF2C* follow an autosomal dominant inheritance pattern and are estimated to contribute to

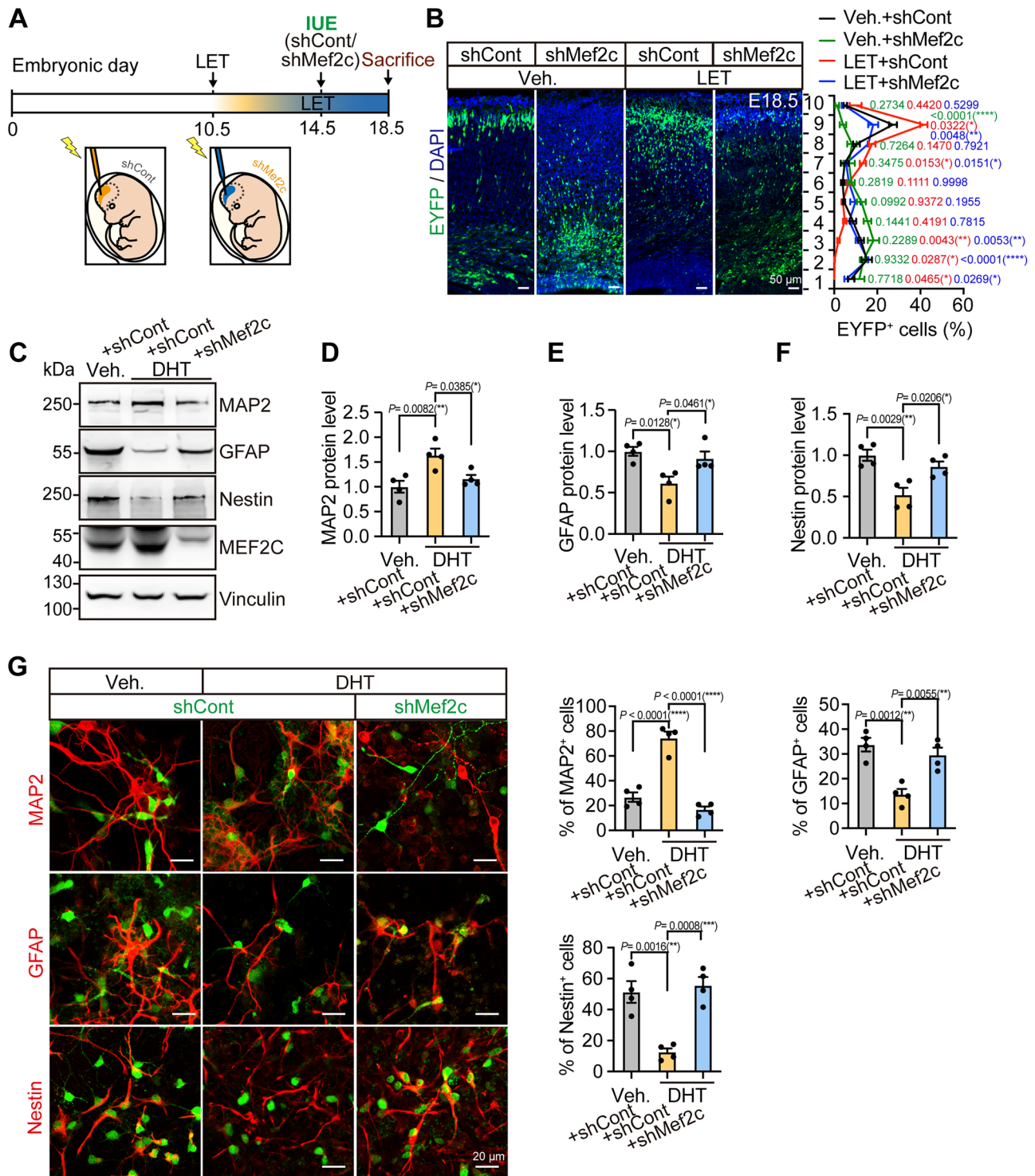
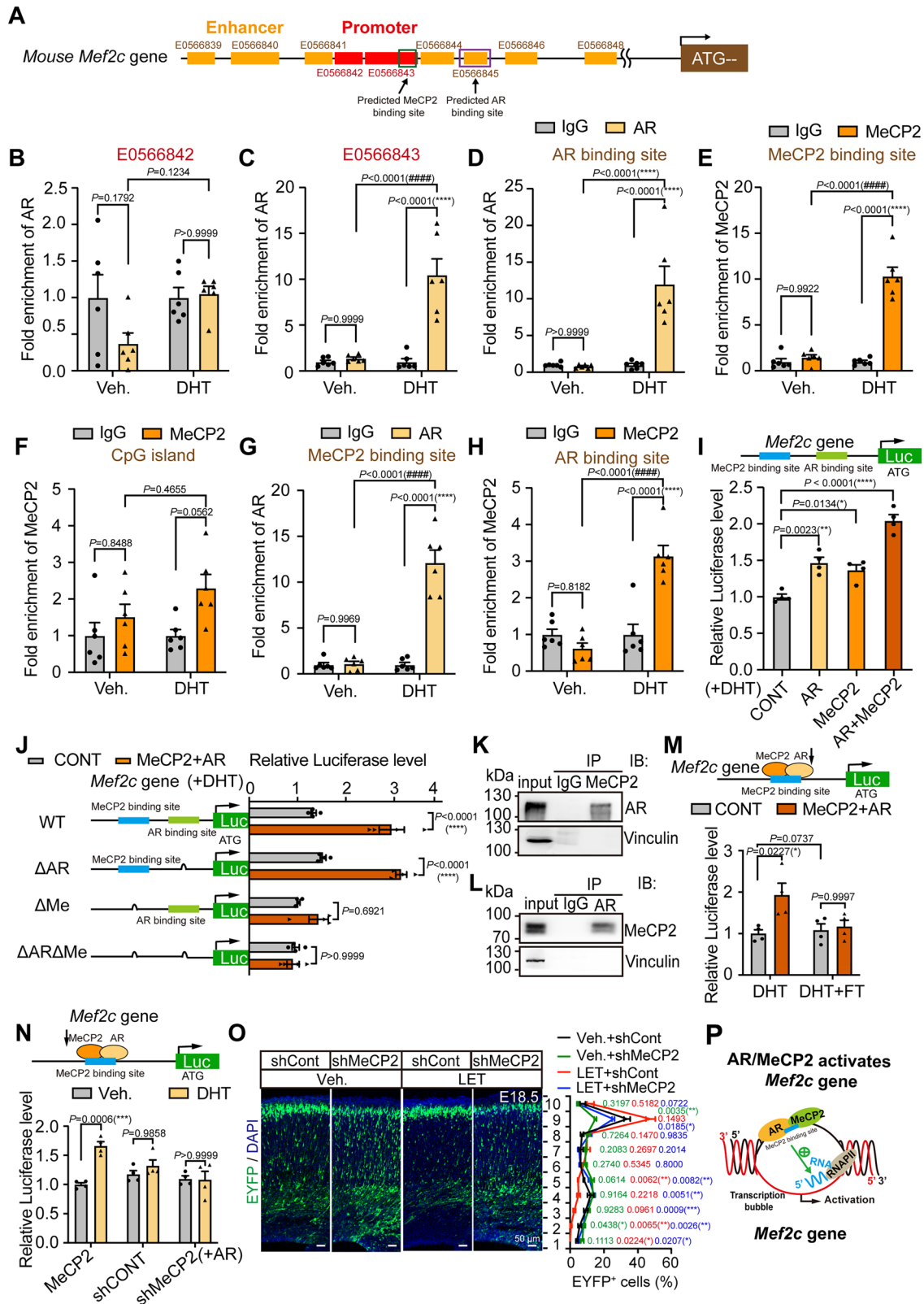


Fig. 5 | Downregulating Mef2c can reverse for the enhanced neurogenesis in male offspring promoted by maternal hyperandrogen. A Schematic of the IUE workflow and treatment timeline. At E14.5, vehicle- (Veh.) or letrozole- (LET) treated embryos were electroporated with an EYFP plasmid carrying either scramble shRNA (shCont) or *Mef2c* shRNA. **B** Cortical tissues were collected at E18.5 from male embryos for immunostaining ($N=4$ males from 4 dams per group). Representative confocal images (left) and quantification of EYFP+ cell distribution across cortical layers (right) are shown. Scale bar, 50 μm . Green, red, and blue asterisks indicate comparisons between Veh. + shCont vs Veh. + shMef2c, Veh. + shCont vs LET + shCont, and LET + shCont vs LET + shMef2c, respectively. **C–F** Mouse primary NPCs were infected with shCont or shMef2c lentivirus and treated with DMSO or

DHT (10 nM). Western blotting was performed to assess MAP2, GFAP, Nestin, and MEF2C levels ($N=4$ per group). Vinculin served as the loading control. Representative blots are shown in (C), and quantification in (D–F).

G Immunofluorescence staining of MAP2, GFAP, and Nestin in NPCs infected with EGFP-expressing shCont or shMef2c viruses. Representative images (left) and quantification of marker-positive cells among EGFP+ cells (right) are shown ($N=4$ independent cultures). Scale bar, 20 μm . All data are expressed as the means \pm SEM. Exact P -values are indicated. * $P < 0.05$; ** $P < 0.01$; *** $P < 0.001$; **** $P < 0.0001$. Two-way ANOVA followed by Sidak *post-hoc* test was performed for (B). One-way ANOVA followed by Tukey *post-hoc* test was performed for (D–G).



approximately 1.1% of ASD/ID cases^{42–45}. A set of rare disorders arising from *MEF2C* haploinsufficiency is collectively termed *MEF2C* haploinsufficiency syndrome (MHS), which is typically caused by heterozygous deletions at the 5q14.3 locus that encompass *MEF2C* or by loss-of-function mutations in *MEF2C*⁴⁵. Initially recognized in 2009 as a 5q14.3 microdeletion syndrome, this disorder was later linked to *MEF2C* haploinsufficiency⁴⁶. Core clinical manifestations of MHS

comprise severe global developmental delay, absent or profoundly impaired speech, hypotonia, epilepsy, stereotypic repetitive behaviors, and prominent neurobehavioral abnormalities^{41,47–49}. Furthermore, a recent systematic review of 117 individuals with *MEF2C* haploinsufficiency indicated that autism-related features and behavioral abnormalities were consistently observed across multiple studies⁵⁰, reinforcing autism-like phenotypes as a key characteristic of

Fig. 6 | AR upregulates *Mef2c* in a MeCP2-dependent manner. **A** Schematic of the *Mef2c* locus showing predicted MeCP2 (green box) and AR (purple box) binding sites, promoter regions (red), and proximal enhancers (orange). **B–D** ChIP-qPCR analysis of AR enrichment at *Mef2c* promoter regions and predicted AR binding sites in N2a cells treated with vehicle or DHT ($N = 6$). **E, F** ChIP-qPCR analysis of MeCP2 enrichment at the *Mef2c* promoter CpG island and predicted MeCP2 binding site ($N = 6$). **G, H** ChIP-qPCR showing AR occupancy at the MeCP2 binding site (**G**) and MeCP2 occupancy at the AR binding site (**H**) following vehicle or DHT treatment ($N = 6$). **I** Luciferase reporter assay in N2a cells co-transfected with pGL3-*Mef2c*-WT and MeCP2, AR, or both, showing regulatory effects on *Mef2c* transcription. **J** Luciferase activity following MeCP2 and AR co-transfection with pGL3-*Mef2c*-WT or different deletion reporters in DHT-treated cells. **K, L** Co-immunoprecipitation of MeCP2 and AR in DHT-treated N2a cells. Vinculin served as a negative control. **M** MeCP2 and AR enhanced luciferase activity in cells expressing

pGL3-*Mef2c*- Δ AR was blocked by flutamide ($N = 4$). **N** Luciferase activity of the pGL3-*Mef2c*- Δ AR reporter could not be enhanced by AR without MeCP2 after DHT treatment ($N = 4$). **O** The cerebral cortex from vehicle or letrozole treated offspring were electroporated with EYFP with either scramble shRNA (shCont) or MeCP2 shRNA at E14.5 and collected from male offspring at E18.5 for sectioning and immunostaining. Scale bars: 50 μ m. The distribution of EYFP⁺ cells in each zone were quantified and shown in the right. $N = 4$ male offspring from 4 dams. Green line: shCont + Veh vs shMeCP2 + Veh; red line: shCont + Veh vs shCont + LET; blue line: shCont + LET vs shMeCP2 + LET. **P** Schematic illustration of the mechanism of AR/ MeCP2 regulation on *Mef2c*. All data are expressed as the means \pm SEM. Exact P -values are indicated. * $P < 0.05$; ** $P < 0.01$; *** $P < 0.001$; **** $P < 0.0001$; ### $P < 0.001$; #### $P < 0.0001$. Two-way ANOVA followed by Sidak *post-hoc* test was performed for (**B–H, J** and **M–O**). One-way ANOVA followed by Tukey *post-hoc* test was performed for (**I**).

this syndrome. Patients with 5q14.3 duplication also show abnormal brain development, including microcephaly and mild ventriculomegaly^{47,48}. These studies reinforced the importance of MEF2C in brain development. However, no sex bias has been reported in these studies. Other human studies on *MEF2C* focused on rare deleterious mutations in the coding region, also revealed no difference in prevalence between males and females with *MEF2C* mutations^{47,51,52}. Interestingly, a recent study by Lombardo et al. highlighted the potential importance of *MEF2C* in the male bias observed in autism²⁰. They found that MEF2C is upregulated in DHT-treated human neural stem cells (hNSCs) and upregulated in human induced pluripotent stem cells (hiPSCs) derived from male autism patients. Their finding is in good agreement with our observations in mice. Our discovery of the AR/MeCP2 regulation in the promoter region of *Mef2c* suggests a possible sex preference through transcriptional regulation. Therefore, it would be interesting to investigate whether there is a sex-related difference in mutation frequencies within this promoter region in future genetic analyses.

A very unexpected finding is that AR does not target *Mef2c* via the canonical AR binding site ARE. Normally, upon binding with androgen, AR is translocated to the nucleus and binds to AREs on its targeted genes^{53,54}. However, our study unravels a form of regulation of AR on its target gene, which is not ARE-dependent. MeCP2 plays an essential role as a transcriptional cofactor in AR-dependent regulation of *Mef2c*. It would be interesting to investigate whether there are other genes that can be regulated by AR in such a non-ARE regulatory pathway. This will enhance our comprehension of how sex hormones regulate gene expression and their roles in sex-specific diseases.

Moreover, our study elucidates that AR binds to MeCP2 and targets the *Mef2c* gene via the MeCP2 binding site. This observation establishes a connection between AR and MeCP2. It would be interesting to investigate whether there are other genes that can be targeted by AR and MeCP2 together and their dual effects on neurodevelopmental conditions. Notably, the MECP2 gene is situated on the X chromosome. Consequently, this dual regulation by AR and MeCP2 may introduce increased complexity into the neurodevelopmental process governed gene-endocrine interactions. In males, MeCP2 mutations can either amplify or negate the effects of hyperandrogenism, depending on the specific nature of the mutation. If a mutation in MeCP2 leads to reduced expression or weakened interaction with AR, it may attenuate androgen effects. Conversely, if a mutation results in increased expression of MeCP2 or enhanced interaction with AR, it could potentiate androgen effects. In addition, females should also be investigated. For example, Rett Syndrome, caused by mutations in the *MECP2* gene, predominantly affects females, as males with MECP2 mutations often exhibit more severe phenotypes and reduced viability⁵⁵, which contributes to the higher prevalence in females.

In our study, no significant behavioral alteration was observed in female offspring. This result aligns with previous findings in aromatase-knockout mouse models, where the most consistent and

pronounced phenotypes in females are largely restricted to the reproductive and endocrine systems, rather than overt neurobehavioral deficits. Specifically, female aromatase-knockout mice exhibit arrested folliculogenesis, absence of corpora lutea, ovarian cyst-like structures, and infertility, all attributable to estrogen deficiency^{56,57}. Neurobehavioral outcomes in these female mice have not been thoroughly characterized. In contrast, Tsuda et al.⁵⁸ used a long-term social preference paradigm to systematically assess male mice with knockouts of aromatase, estrogen receptor α or β , or oxytocin-related genes, and demonstrated that aromatase deficiency results in consistent and reproducible alterations in social preference in males. It should be noted that their study did not include female subjects. Furthermore, Hu et al.⁵⁹ conducted a systematical investigation of sex differences in ROR α expression and its transcriptional targets in human and mouse brains, revealing sexually dimorphic expression of several ROR α target genes, including *CYP19A1* (which encodes aromatase), in specific brain regions. In the mouse cortex, correlations between ROR α expression and its targets, such as *Cyp19a1*, were significantly stronger in males than in females, suggesting a more tightly coordinated transcriptional regulatory network in the male brain. In human cortical tissue, a strong positive correlation between ROR α and aromatase protein levels was observed in control individuals and males with ASD, whereas this correlation was absent in females with ASD. This finding points to a sex-specific disruption of steroidogenic transcriptional regulation in autism. Together, these findings support a potential role of aromatase in the sex-biased susceptibility to neurodevelopmental conditions.

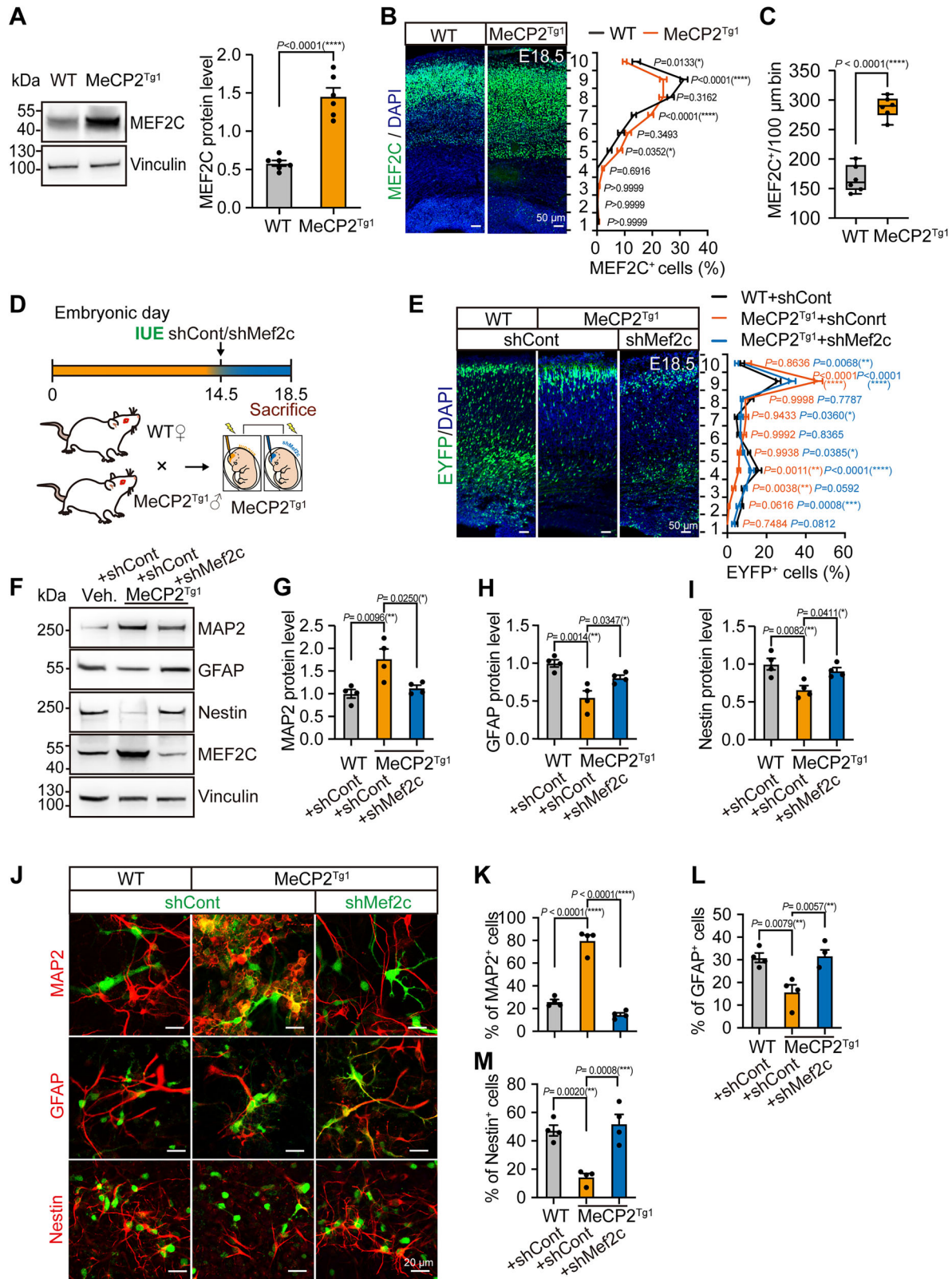
Notably, androgen exposure in our model did not result in detectable whole-brain enlargement (Supplementary Fig. S2N, O). This finding aligns with clinical imaging studies, which indicate that brain overgrowth is observed only in a subset of individuals with autism spectrum disorder^{60,61}. Furthermore, increased brain volume in autism is more commonly reported during early postnatal development rather than during the prenatal period^{62–64}. Collectively, these results suggest that prenatal androgen exposure may primarily influence specific developmental processes, such as cortical neurogenesis, without causing generalized changes in total brain size.

In summary, we have uncovered a previously unrecognized MeCP2-dependent regulatory pathway downstream of AR in cortical neurogenesis in males. Our results elucidate the effects of gene-maternal endocrine interactions on cortical development, which may help to explain the sex differences associated with early-onset neurodevelopmental conditions such as autism.

Methods

Mice, cell lines and cell culture

FVB-Tg (*MECP2*)1Hzo/J (MeCP2^{Tg1}) mice were maintained in the animal facility at the Institute of Developmental Biology & Molecular Medicine, Fudan University. All mice were maintained in a Specific Pathogen Free (SPF) facility, a HEPA-filtered room and using a



Tecniplast individually ventilated caging system / room. The room has controlled temperature (20–22 °C), humidity (30–70%) and light (12 h light-dark cycle). Mice were fed a standard irradiated rodent chow diet (Xietong Bioengineering, Jiangsu, China; Catalog No. XT101FZ-010) and had ad libitum access to food and water. The genotyping of MeCP2^{Tg1} mice were determined by PCR following the protocols from the Jackson Laboratory.

This study was carried out in strict accordance with the recommendations in the Guide for the Care and Use of Laboratory Animals of Fudan University (IDM2021044a). The protocol was approved by the Committee on the Ethics of Animal Experiments of Fudan University. For all animal procedures, including tissue collection and primary cell isolation, mice were deeply anesthetized with isoflurane (2-3% in oxygen) and subsequently euthanized by cervical dislocation. For the IUE

Fig. 7 | Downregulating *Mef2c* counteracts the enhanced cortical neurogenesis induced by *MeCP2* duplication. **A** MEF2C protein level in the embryonic cortices of WT and *MeCP2*^{Tg1} male mice were detected by western blot. Vinculin served as the loading control in the Western blot. (*N* = 6 males from 4 dams). **B, C** MEF2C⁺ cell distribution in the embryonic cortices of WT and *MeCP2*^{Tg1} male mice were detected by immunofluorescence staining. (*N* = 6 males from 6 dams). MEF2C⁺ cell distribution across 10 cortical bins is shown in **(B)**, and total MEF2C⁺ cell counts per 100 μm bin are quantified in **(C)**. Scale bars, 50 μm. **D, E** EYFP and either shCont or *Mef2c* shRNA were introduced into the cerebral cortex of WT or *MeCP2*^{Tg1} embryos via IUE at E14.5 **(D)**. Tissues were collected at E18.5 for immunostaining. **(E)** Distribution of EYFP⁺ cells across cortical zones was analyzed (*N* = 6 male offspring from 4 dams). Scale bars, 50 μm. Orange and blue labels denote comparisons between WT vs *MeCP2*^{Tg1} (shCont) and *MeCP2*^{Tg1} (shCont) vs *MeCP2*^{Tg1} (sh*Mef2c*), respectively. **F–I** Primary NPCs from WT or *MeCP2*^{Tg1} embryos were infected with

shCont or sh*Mef2c* lentivirus. Protein levels of MAP2, GFAP, Nestin, and MEF2C were assessed by western blot (*N* = 4 independent cultures), with Vinculin as the loading control. Representative blots are shown in **(F)**, and quantification in **(G–I)**.

J–M Immunofluorescence staining for MAP2, GFAP, and Nestin in NPCs infected with EGFP-labeled shCont or sh*Mef2c* lentivirus. Marker-positive cells within the EGFP⁺ population were quantified (*N* = 4 independent cultures). Representative images are shown in **(J)**; quantification is shown in **(K–M)**. Scale bar, 50 μm. All data are expressed as the means ± SEM. Box plots show the median (center line), 25th–75th percentiles (box limits), and whiskers indicate the minimum and maximum values. Exact *P*-values are indicated. **P* < 0.05; ***P* < 0.01; ****P* < 0.001; *****P* < 0.0001. Statistical analyses were performed using two-tailed unpaired Student's *t* test **(A, C)**, two-way ANOVA with Sidak's *post hoc* test **(B, E)**, or one-way ANOVA with Tukey's *post hoc* test **(G–I, K–M)**.

experiment and intraventricular injections of letrozole or flutamide, pregnant mice were anesthetized with pentobarbital sodium (50 mg/kg, administrated via intraperitoneal injection).

Letrozole (LET, HY-14248, Medchemexpress) was dissolved in 20% ethanol in corn oil at a concentration of 1 μg/ml. Pregnant mice of the treatment group were subcutaneously injected with LET dissolved in corn oil at a dosage of 1 μg/kg once daily for eight days (from E10.5 to E17.5), while control mice received only the vehicle (corn oil only) accordingly.

N2a cell line (mouse neuroblastoma, male origin) was cultured with DMEM supplemented with 10% fetal bovine serum and penicillin/streptomycin (100 units per 100 μg/ml) in a 5% CO₂ incubator at 37 °C. Transfection was performed using FuGENE (Roche, 14738300) transfection reagent according to the manufacturer's protocol. When the confluency of adherent cells reached 70%, the cells were treated with 10 nM DHT (Selleck, 521-18-6), 10 nM DHT + 0.4 μM flutamide (Aladdin, 13311-84-7) or vehicle (DMSO) (distilled water) for 24 h. Each treatment was replicated at least three times. N2a cells were either lysed for the Luciferase Reporter Assay or subjected to Chromatin Immunoprecipitation (ChIP) PCR assay. Firefly luciferase and Renilla luciferase activities were determined using the Luciferase Assay Reagent and Renilla Luciferase Assay (Promega), respectively.

HI human embryonic stem cells (male origin) were maintained in mTeSRTM1 medium (STEMCELL Technologies, 85850) on culture plates coated with Corning[®] Matrigel[®] (356277). Cells were dissociated into single cells using ACCUTASE[™] (STEMCELL Technologies, 07920) and replated for neural induction. Neural differentiation was initiated by replacing the culture medium with STEMdiff[™] Neural Induction Medium (STEMCELL Technologies, 05839). Cells were cultured under standard conditions for 7 days, with daily medium changes, to generate neural stem cells (NSCs). Subsequently, NSCs were further induced toward neuronal differentiation by switching to Neurobasal medium (Thermo Fisher Scientific) supplemented with 2% B27 (v/v; Thermo Fisher Scientific), GlutaMAX (Thermo Fisher Scientific), brain-derived neurotrophic factor (BDNF, 50 ng/mL), glial cell line-derived neurotrophic factor (GDNF, 50 μg/mL), and 1% penicillin–streptomycin (Thermo Fisher Scientific). During the neuronal differentiation stage, cells were treated with dihydrotestosterone (DHT, 10 nM) alone or with DHT in combination with the androgen receptor (AR) antagonist flutamide (0.4 μM). Vehicle control cells received an equivalent volume of DMSO. After 7 days of treatment, cells were harvested for Western blot analysis or subjected to immunofluorescence staining.

Immunofluorescent staining

For immunostaining of tissue sections, fresh offspring brains were fixed with 4% paraformaldehyde, cryoprotected in sucrose and embedded in O.C.T. compound. Sections were prepared at 20 μm thickness on Leica CM1900 Microtome, and then blocked and permeabilized with the blocking solution (10% goat serum and 0.5% Triton X-100, in PBS), followed by incubation with primary antibodies and secondary antibodies. Primary antibodies used were mouse anti-MAP2

(Abcam, ab11268, 1:500), rabbit anti-GFAP (Abcam, ab7260, 1:1000), rabbit anti-SOX2 (Abcam, ab97959, 1:500), rabbit anti-SATB2 (Abcam, ab92446, 1:100), rabbit anti-TBR1 (Abcam, ab183032, 1:100), rabbit anti-EAAT1 (Abcam, ab181036, 1:100), rabbit anti-Nestin (Abcam, ab6142, 1:1000), rabbit anti-TBR2 (Abcam, ab23345, 1:300). Appropriate secondary antibodies used were Alexa Fluor[®] 647-labeled goat anti-Rabbit (Abcam, ab150079, 1:500), Alexa Fluor[®] 647-labeled goat anti-mouse (Abcam, ab150115, 1:500), Alexa Fluor[®] 488-labeled goat anti-Rabbit (Abcam, ab150077, 1:500) and Alexa Fluor[®] 488-labeled goat anti-mouse (Abcam, ab150117, 1:500). DAPI (Sigma-Aldrich) was used to stain nuclei. Stained sections were subjected to imaging with a Zeiss LSM700 microscope.

Isolation and differentiation assay of primary mouse NPCs

NPCs were isolated from the cortex of E12.5–14.5 WT or *MeCP2*^{Tg1} mouse embryos. NPCs were isolated and cultured in Neurobasal medium (ThermoFisher) containing 40 ng/ml bFGF (Peprotech), 2% B27 (v/v, ThermoFisher), GlutaMAX (ThermoFisher) and 1% penicillin and streptomycin (ThermoFisher). NPCs were infected with different lentivirus (Obio Technology (Shanghai) Corp., Ltd.). 4 days later, NPCs cells were either lysed for western blot or subjected to immunofluorescent staining.

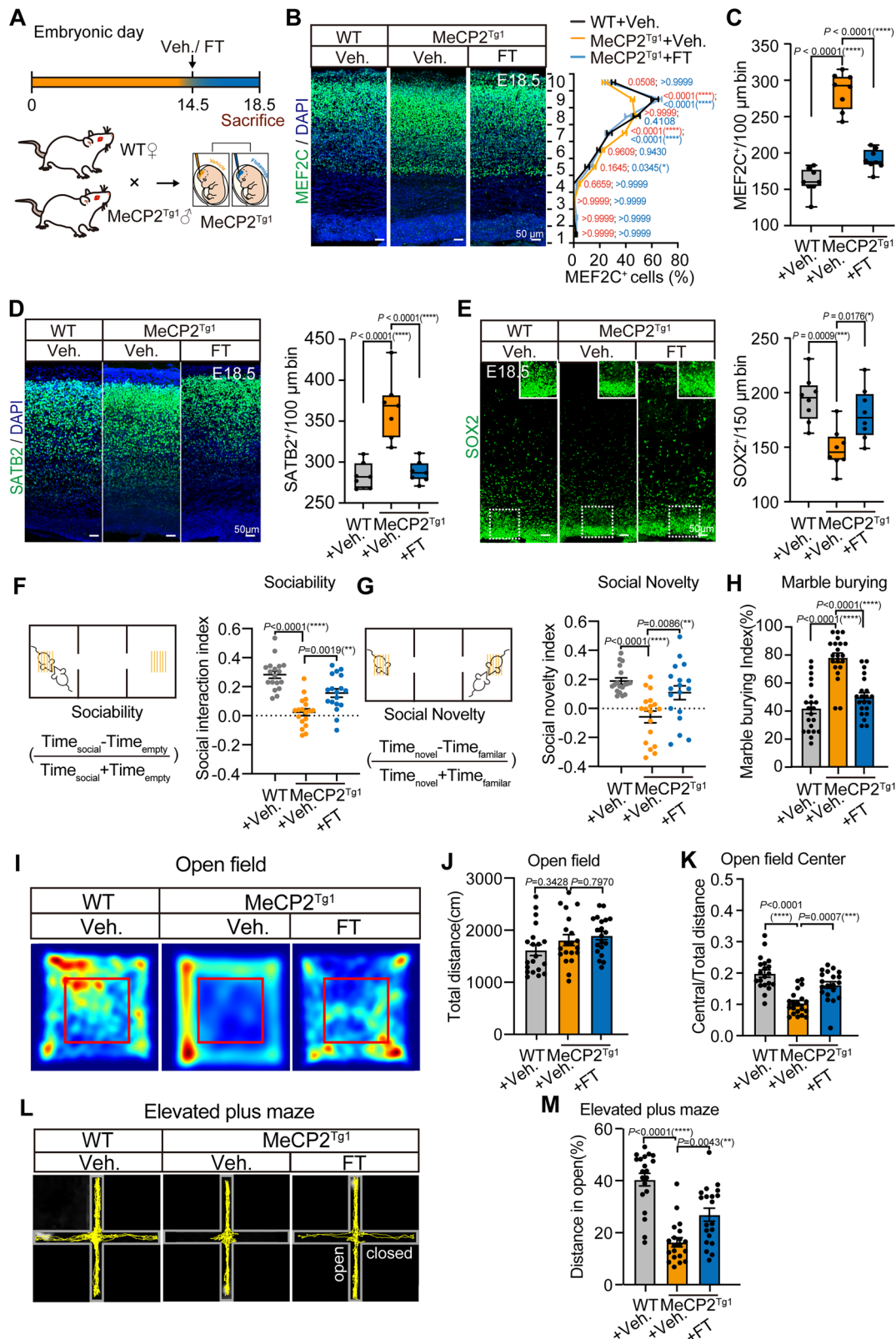
qRT-PCR and western blot

Total RNA from cerebral cortex or N2a cells was extracted with TRIzol (Invitrogen) and reverse transcribed (Toyobo, FSQ-301) for qRT-PCR. Real-time PCR was performed using Realtime PCR Master Mix (Toyobo, QPK-101). Relative expression of each target gene was calculated by comparison to the expression of mouse *Gapdh*. The detailed information of primers is listed in Supplementary Table S2.

For western blot, cells were homogenized in ice-cold RIPA buffer and centrifuged at 12,000 × *g*. The supernatant was resolved by 10% SDS-PAGE, electro-transferred to a PVDF membrane, and probed with the following antibodies: rabbit anti-MAP2 (Abcam; ab32454; 1:1000), rabbit anti-GFAP (Abcam; ab7260; 1:2000), rabbit anti-Nestin (Abcam; ab6142; 1:1000), rabbit anti-Androgen Receptor (Abcam; ab108341; 1:1000), rabbit anti-MEF2C (Abcam; ab211493; 1:1000), rabbit anti-Vinculin (Abcam; ab129002; 1:5000) and goat anti-rabbit IgG-HRP (Abcam; ab97051; 1:5000) antibodies. Blotting images were acquired with a Tanon-5200 imaging system. Densitometric quantification of the target protein was determined by Image J and compared with the internal control to determine the relative expression value. The internal control was Vinculin. The representative blots were selected from at least three repeated experiments.

Co-immunoprecipitation and immunoblotting

The N2a cells transfected with *MeCP2* and AR and treated with DHT were lysed with SDS lysis buffer at 4 °C for 10 min. Lysates were incubated overnight at 4 °C with anti-*MeCP2* antibody (Abcam, ab2828) or Rabbit IgG (Cell Signaling, Cat# 3900), and then with Protein A + G



Agarose beads (Santa Cruz Biotechnology, Cat# sc-2003) at 4 °C for 2h. Subsequently, immunoprecipitants were washed three times, equivalent amounts of protein were detected by western blot with rabbit anti-MeCP2 antibody (Cell Signaling Technology; Cat# 3456; 1:1 000), rabbit anti-Androgen Receptor (Abcam; ab108341) or rabbit anti-Vinculin (Abcam; ab129002). To assess the interaction between MeCP2 and AR under hyperandrogen conditions, cells were treated with DHT

prior to lysis. Co-IP experiments were also conducted without DHT treatment to determine if MeCP2 and AR interact at baseline conditions.

ELISA

Mouse serum (20 μL) was collected and diluted with PBS at a ratio of 1:19. Amniotic fluid (20 μL) was collected and diluted with PBS at a ratio

Fig. 8 | Blocking AR rescues the enhanced cortical neurogenesis and autistic behavior in male offspring caused by MeCP2 duplication. **A** Schematic of the experimental design and flutamide (FT) treatment timeline. WT and MeCP2^{Tg1} male embryos were injected intracerebrally at E14.5 with vehicle (10% DMSO in saline) or FT (0.6 μg), and analyzed at E18.5. **B, C** Immunofluorescence of MEF2C⁺ cells in the cerebral cortex of vehicle-treated WT, vehicle- and FT-treated MeCP2^{Tg1} mice. **B** Representative images and distribution of MEF2C⁺ cells across 10 cortical bins ($N = 6$ males from 6 dams per group). **C** Quantification of MEF2C⁺ cell number per 100 μm bin ($N = 8$ males from 6 dams per group). Scale bars, 50 μm. Red and blue labels indicate comparisons between WT + Veh. vs MeCP2^{Tg1} + Veh. and MeCP2^{Tg1} + Veh. vs MeCP2^{Tg1} + FT, respectively. **D** Immunostaining and quantification of SATB2⁺ upper-layer neurons in the cortex ($N = 7$ males from 6 mothers per group). Scale bar, 50 μm. **E** SOX2⁺ progenitor cells were analyzed in vehicle- and FT-treated MeCP2^{Tg1} cortices ($N = 8$ males per group). Representative images and high-

magnification views of boxed areas are shown. Quantification was based on cell counts per 150 μm bin. **F, G** Three-chamber social interaction (**F**) and social novelty (**G**) tests. Diagrams are shown on the left, and quantifications are shown on the right. $N = 18$ males from 10 dams per group. **H** Marble burying index, calculated as the proportion of buried marbles ($N = 21$ males from 10 dams per group). **I–K** Open field test: representative locomotor heatmaps (**I**), total distance traveled (**J**), and center/total distance ratio (**K**), $N = 20$ males from 10 dams per group. **L, M** Elevated plus maze test: representative locomotion tracks (**L**) and quantification of open arm distance (**M**) ($N = 20$ males from 10 dams per group). Data are presented as mean ± SEM. Box plots show the median (center line), 25th–75th percentiles (box limits), and whiskers indicate the minimum and maximum values. Exact P -values are indicated. Statistical analyses were performed using two-way ANOVA test followed by Sidak *post-hoc* test for (**B**), and one-way ANOVA followed by Tukey *post-hoc* test for (**C–H, J, K** and **M**). * $P < 0.05$; ** $P < 0.01$; *** $P < 0.001$; **** $P < 0.0001$.

of 1:4. The total testosterone was measured in the media by Testosterone ELISA Kit (Abnova, KA0309). Serum estradiol was detected by Elabscience[®] Human/Monkey/Mouse E2 (Estradiol) ELISA Kit (E-EL-0150c). Each experiment was conducted in triplicate, with three wells per treatment in each experiment.

In utero electroporation and intraventricular injections of flutamide

In utero electroporation was performed at embryonic day 14.5 (E14.5). Pregnant mice were anesthetized with pentobarbital sodium (50 mg/kg, administrated via intraperitoneal injection) and the uterine horns were exposed, and about 1.5 μl of plasmid DNA was then injected into the lateral ventricles of intrauterine embryos, and electronic pulses (35 V, 50 msec, 4 or 5 times) were applied using an electroporator with a forceps-type electrode. The embryos were allowed to live within the uterine horn until the desired time of observation.

For intraventricular injections, WT or MeCP2^{Tg1} pregnant mice at E14.5 were anesthetized, and the uterine horns were exposed and about 1.5 μl of flutamide (0.4 μg/μl) or vehicle (10% DMSO in saline) were injected.

The percentage of EYFP⁺ cells in each bin was calculated based on the total number of EYFP⁺ cells in the same brain section. At least three sections from one brain were collected, and at least four different embryos obtained from three to four different pregnant dams were collected for each group for statistical analyses.

Behavioral studies

All mice in the behavioral experiments were aged 7–8 weeks and were handled for 5 days before the behavioral tasks took place. All home cages containing mice were transported to the testing room at least 60 min before the start of testing. In addition, mice were allowed to freely move and explore the apparatus during the behavioral task. Behavioral tests were all conducted from 9:00 to 18:00, which was in the light phase of the light-dark cycle.

Three-chamber social interaction and social novelty test. The three-chambered test was conducted in the behavioral apparatus made of transparent plastic board with dimensions of 60 × 45 × 22 cm³, featuring a 20 cm-wide center chamber and two 20 cm-wide side chambers under dim-light conditions (15–16 lux). The apparatus included dummy plates with 7 × 10 cm² cut-out doors, ensuring unrestricted movement between chambers. The two-sided chambers contained small plastic cages to house social partner mice. One day before the test, mice were habituated to the apparatus using empty cages in both chambers for 60 min, while social partner mice (unfamiliar FVB/NTac male mice) were placed in the plastic cages for 60 min to relieve tension and anxiety. Each trial comprised three sessions: habituation, social approach, and social novelty. On the test day, each mouse was put into the center chamber of the apparatus and allowed to move freely to adequately explore all three

chambers during the habituation session. On the social approach session, the same test mouse was placed into the center chamber while a social partner mouse (stranger #1) was placed into the iron cage on either of the side chambers and subsequently allowed to move freely to explore the apparatus for 10 min. On the social novelty session, the same test mouse was returned to the center chamber while a new stranger mouse (stranger #2) was placed into the other side chamber and allowed to move freely for 10 min. The entire apparatus was wiped with deodorizer between each trial to eliminate olfactory cues between animals. The time spent interacting with a social partner mouse or empty cage, and locomotion heatmaps were analyzed with the Ethovision XT software (Noldus) and visualized through ImageJ. A sociability index was calculated as the time spent with the mouse cup minus time spent with the empty cup divided by the total time of investigation ($\frac{Time_{social} - Time_{empty}}{Time_{social} + Time_{empty}}$). Accordingly, the sociability index during the social novelty phase (Novelty index) was calculated as the time spent with the novel mouse cup minus time spent with the familiar mouse cup divided by the total time of investigation ($\frac{Time_{novel} - Time_{familiar}}{Time_{novel} + Time_{familiar}}$).

Marble-burying (MB) assay. One week following the social approach task, male mice were acclimated for 0.5–1 h in separate clean holding cages. Subsequently, mice were introduced to a testing arena with dimensions of 22 × 15 × 15 cm³ and a bedding depth of 4 cm. The arena contained 24 glass marbles arranged in four rows of six marbles, equidistant from each other. After a 30 min exploration period, mice were gently removed from the testing cages, and the number of marbles buried was meticulously recorded. The scoring was based on the number of marbles buried, with a criterion of more than 50% of the marble's volume covered by bedding material for each mouse.

Open field (OF) test. The open field test was conducted using a plastic board measuring 40 × 40 × 40 cm³. Each mouse was centrally placed within the apparatus and given 20 min to freely explore. Movement time, total distance traveled, and distance covered in the central zone (20 × 20 cm²) were video-recorded and subsequently analyzed using EthoVision XT software (Noldus). The center distance ratio was computed as the distance traveled by the mouse in the center relative to the total distance covered.

Elevated plus maze test. The elevated plus maze test was performed in a dedicated behavioral apparatus, featuring closed arms composed of a plastic board measuring 30 × 6 × 15 cm³, and open arms measuring 30 × 6 × 0.5 cm³, with the entire apparatus reaching a height of 50 cm. Each test mouse was positioned in the central area of the plus maze and allowed 10 minutes of unrestricted movement to thoroughly explore the entire maze. The distance traveled in both the open and closed arms, along with data analysis, was conducted using EthoVision XT software and visualized using ImageJ.

Chromatin immunoprecipitation (ChIP) PCR assay

The N2a cells treated with vehicle or DHT was cross-linked with 1% formaldehyde at 37 °C for 25 min. The reaction was stopped with 0.2 M glycine for 10 min at room temperature (RT), and then the cells were sedimented, washed, homogenized, and lysed with SDS lysis buffer at 4 °C for 10 min. The lysates were sonicated to reduce DNA lengths in the ice and were subjected to the chromatin immunoprecipitation assay using the previously described protocols. Cross-linked protein-DNA complexes were immunoprecipitated by incubation with antibodies, including rabbit anti-Androgen Receptor (Abcam; ab108341), rabbit anti-MeCP2 (Abcam, ab195393) and rabbit IgG (negative control) antibodies overnight, and then with Protein A + G Agarose beads at 4 °C for 2 h. DNA was thereafter purified from the mixture. The DNA fragments were quantitatively amplified by real-time PCR. The detailed information of primers is listed in Supplementary Table S3.

Plasmid construction

The AR expression plasmid containing mouse *Ar* cDNA was amplified by PCR and subcloned into the *Xho*I/*Sal*I sites of the pCMS-EGFP plasmid. Four different regions of the mouse *Mef2c*-promoter were cloned into *Xba*I/*Fse*I sites of a pGL3-control plasmid to generate luciferase reporter constructs. *Mef2c*-WT contains the *Mef2c* promoter, which covers the predicted MeCP2 binding site and predicted AR binding site. The double deletion reporter *Mef2c*- Δ AR Δ Me which deleted both of the MeCP2 binding site and the predicted AR binding site of the *Mef2c* promoter. The single deletion reporters *Mef2c*- Δ AR and *Mef2c*- Δ Me, which deleted the MeCP2 binding site or the predicted AR binding site of the *Mef2c* promoter. The sequences of different regions of the mouse *Mef2c*-promoter are listed in Supplementary Table S4. The plasmid and the lentivirus for sh*Mef2c* and shCont were all purchased from GenePharma (Shanghai, China). The sequences of sh*Mef2c* are listed in Supplementary Table S5. The mouse MeCP2 shRNA was directed against the sequence as follows: 5'-AAGTCAGAAGACCAGGATC-3', was based on previously published literature⁶⁵. The sequences of AR shRNA are as reported previously²⁹. The sense oligonucleotide sequence is: 5'-GATCCTATCCCAGTCCCACTTGATCGAGCAAGTGGGACTGGGATAGGGCTTTTT-3', and the antisense oligonucleotide sequence is: 5'-AGCTAAAAGCCCTATCCAGTCCCACTTGCTCGATCAAGTGGGACTGGGATAG-3'. The AR-V7 expression plasmid containing *AR-V7* cDNA were all purchased from Obio Technology (Shanghai) Corp., Ltd.

RNA sequencing

We harvested and flash-froze cerebral cortex from E17.5 cortical tissue derived from offspring of maternal hyperandrogenic conditions and control mice ($N=3$ per sex per group), and extracted total RNA using TransZol Up Plus RNA Kit (ERS01-01, Trans). Individual biological replicates then underwent library preparation and sequencing. Library preparation was performed by SHBIO Biotechnology Corporation (Shanghai, China). Agilent Bioanalyzer 2100 (Agilent Technologies, Santa Clara, CA, US) was used to assess the quality and integrity of RNA. VAHTS Universal V6 RNA-seq Library Prep Kit for Illumina® (Vazyme) was used to prepare libraries, following the manufacturer's instructions. The Illumina Novaseq6000 instrument was used for sequencing. The original RNA-seq data have been deposited in the NCBI Sequence Read Archive, accession number: PRJNA1031421.

RNA-seq data analysis and identification of DE Genes

RNA-seq data were processed and analyzed using standard bioinformatics pipelines. Differential expression analysis was performed using DESeq2, which models count data from RNA-seq experiments and tests for differential expression by using a negative binomial generalized linear model. DESeq2 provides robust statistical methods to handle the large number of comparisons inherent in RNA-seq data. We identified differentially expressed (DE) genes based on both statistical significance and

fold change. Specifically, genes were considered DE if they had an adjusted p-value (false discovery rate, FDR) of less than 0.05 and an absolute log fold change (log FC) greater than 0.3. The FDR correction for multiple comparisons was implemented using the Benjamini-Hochberg procedure to control the expected proportion of false positives. To further validate the reliability of the screening results and eliminate false positives, we selected several DE genes and performed RT-PCR validation using an additional sample set (four pairs).

Steroid hormone quantification by UHPLC-MS/MS

Steroid hormones in mouse brain tissues were quantified using ultra-high-performance liquid chromatography coupled with tandem mass spectrometry (UHPLC-MS/MS). Approximately 25 mg of tissue was homogenized, extracted with methanol containing internal standards, and subjected to solid-phase extraction. Eluted samples were analyzed on a SCIEX triple quadrupole mass spectrometer operated in multiple reaction monitoring (MRM) mode. Chromatographic separation was performed using a Waters LC column with the column temperature set to 50 °C and an injection volume of 20 μ L. Mass spectrometry was conducted under optimized MRM conditions, and analytes were quantified using calibration curves generated with authentic standards and internal standards. All calibration curves showed correlation coefficients (R^2) > 0.99. The lower limits of quantification ranged from 1 to 5000 pg/mL, and quality control recoveries were between 84% and 119%. Final metabolite concentrations were calculated based on measured concentrations, sample volume, and tissue mass.

Statistical analyses

All experiments were repeated in at least three independent experiments, and statistical significance was evaluated as indicated. Data are presented as mean \pm SEM unless otherwise stated. Sample sizes (N) are reported in the text and figure legends for all experiments, with the unit of analysis clearly specified (e.g., number of dams, offspring, or independent cultures, as appropriate). Statistical differences between two groups were assessed using two-tailed unpaired t tests, whereas comparisons among multiple groups were performed using one-way or two-way analysis of variance (ANOVA), as specified for each experiment. Effect sizes were calculated to complement significance testing, with Cohen's d reported for pairwise comparisons and partial η^2 reported for ANOVA-based analyses. All statistical analyses were conducted using GraphPad Prism (GraphPad Software, La Jolla, CA). A P -value < 0.05 was considered statistically significant.

Reporting summary

Further information on research design is available in the Nature Portfolio Reporting Summary linked to this article.

Data availability

The RNA-seq data generated in this study have been deposited in the NCBI Sequence Read Archive under accession code [PRJNA1031421](https://www.ncbi.nlm.nih.gov/sra/PRJNA1031421). The data supporting the findings of this study are available within the article, its Supplementary Information, and the Source Data files provided with this paper. Source data are provided in this paper.

References

1. Shefcyk, A. Count us in: addressing gender disparities in autism research. *Autism* **19**, 131–132 (2015).
2. Kokras, N. & Dalla, C. Sex differences in animal models of psychiatric disorders. *Br. J. Pharm.* **171**, 4595–4619 (2014).
3. Mottron, L. et al. Sex differences in brain plasticity: a new hypothesis for sex ratio bias in autism. *Mol. Autism* **6**, 33 (2015).
4. Fombonne, E. The epidemiology of autism: a review. *Psychol. Med.* **29**, 769–786 (1999).
5. Saure, E., Castren, M., Mikkola, K. & Salmi, J. Intellectual disabilities moderate sex/gender differences in autism spectrum disorder: a

- systematic review and meta-analysis. *J. Intellect. Disabil. Res.* **67**, 1–34 (2023).
6. Burrows, C. A., Elison, J. T. & Piven, J. Mitigating sex-related biases to elucidate the autism phenotype. *Biol. Psychiatry* **99**, 357–364 (2025).
 7. Burrows, C. A. et al. A data-driven approach in an unbiased sample reveals equivalent sex ratio of autism spectrum disorder-associated impairment in early childhood. *Biol. Psychiatry* **92**, 654–662 (2022).
 8. Werling, D. M. & Geschwind, D. H. Sex differences in autism spectrum disorders. *Curr. Opin. Neurol.* **26**, 146–153 (2013).
 9. Baron-Cohen, S. et al. Why are autism spectrum conditions more prevalent in males? *PLoS Biol.* **9**, e1001081 (2011).
 10. Lombardo, M. V. et al. Fetal programming effects of testosterone on the reward system and behavioral approach tendencies in humans. *Biol. Psychiatry* **72**, 839–847 (2012).
 11. Baron-Cohen, S. et al. Elevated fetal steroidogenic activity in autism. *Mol. Psychiatry* **20**, 369–376 (2015).
 12. Kosidou, K. et al. Maternal polycystic ovary syndrome and the risk of autism spectrum disorders in the offspring: a population-based nationwide study in Sweden. *Mol. Psychiatry* **21**, 1441–1448 (2016).
 13. Cherskov, A. et al. Polycystic ovary syndrome and autism: A test of the prenatal sex steroid theory. *Transl. Psychiatry* **8**, 136 (2018).
 14. Douglas, K. M., Fenton, A. J., Eggleston, K. & Porter, R. J. Rate of polycystic ovary syndrome in mental health disorders: a systematic review. *Arch. Women's. Ment. Health* **25**, 9–19 (2022).
 15. Katsigianni, M., Karageorgiou, V., Lambrinouadaki, I. & Siristatidis, C. Maternal polycystic ovarian syndrome in autism spectrum disorder: a systematic review and meta-analysis. *Mol. Psychiatry* **24**, 1787–1797 (2019).
 16. Auyeung, B., Lombardo, M. V. & Baron-Cohen, S. Prenatal and postnatal hormone effects on the human brain and cognition. *Pflug. Arch.* **465**, 557–571 (2013).
 17. Lombardo, M. V. et al. Fetal testosterone influences sexually dimorphic gray matter in the human brain. *J. Neurosci.* **32**, 674–680 (2012).
 18. Marrocco, J. & McEwen, B. S. Sex in the brain: hormones and sex differences. *Dialogues Clin. Neurosci.* **18**, 373–383 (2016).
 19. Ernst, C. Proliferation and differentiation deficits are a major convergence point for neurodevelopmental disorders. *Trends Neurosci.* **39**, 290–299 (2016).
 20. Lombardo, M. V. et al. Sex-specific impact of prenatal androgens on social brain default mode subsystems. *Mol. Psychiatry* **25**, 2175–2188 (2020).
 21. Quartier, A. et al. Genes and pathways regulated by androgens in human neural cells, potential candidates for the male excess in autism spectrum disorder. *Biol. Psychiatry* **84**, 239–252 (2018).
 22. Kelava, I., Chiaradia, I., Pellegrini, L., Kalinka, A. T. & Lancaster, M. A. Androgens increase excitatory neurogenic potential in human brain organoids. *Nature* **602**, 112–116 (2022).
 23. Xu, X. J. et al. Prenatal hyperandrogenic environment induced autistic-like behavior in rat offspring. *Physiol. Behav.* **138**, 13–20 (2015).
 24. Molyneaux, B. J., Arlotta, P., Menezes, J. R. & Macklis, J. D. Neuronal subtype specification in the cerebral cortex. *Nat. Rev. Neurosci.* **8**, 427–437 (2007).
 25. Gholizadeh, S., Arsenault, J., Xuan, I. C., Pacey, L. K. & Hampson, D. R. Reduced phenotypic severity following adeno-associated virus-mediated Fmr1 gene delivery in fragile X mice. *Neuropsychopharmacology* **39**, 3100–3111 (2014).
 26. Thomas, A. et al. Marble burying reflects a repetitive and perseverative behavior more than novelty-induced anxiety. *Psychopharmacology* **204**, 361–373 (2009).
 27. Peça, J. et al. Shank3 mutant mice display autistic-like behaviours and striatal dysfunction. *Nature* **472**, 437–442 (2011).
 28. Dietrich, W. et al. Testosterone dependent androgen receptor stabilization and activation of cell proliferation in primary human myometrial microvascular endothelial cells. *Fertil. Steril.* **95**, 1247–1255 (2011).
 29. Wang, T. et al. Targeting silencing androgen receptor gene by shRNA with low-intensity focused ultrasonic irradiation inhibits growth of prostate cancer xenografts in nude mice. *Int. J. Clin. Exp. Pathol.* **12**, 1295–1304 (2019).
 30. Kido, T. & Lau, Y. C. Androgen receptor variant 7 exacerbates hepatocarcinogenesis in a c-MYC-driven mouse HCC model. *Oncogenesis* **12**, 4 (2023).
 31. Telley, L. et al. Sequential transcriptional waves direct the differentiation of newborn neurons in the mouse neocortex. *Science* **351**, 1443–1446 (2016).
 32. Wyce, A., Bai, Y., Nagpal, S. & Thompson, C. C. Research Resource: The androgen receptor modulates expression of genes with critical roles in muscle development and function. *Mol. Endocrinol.* **24**, 1665–1674 (2010).
 33. Tu, S. et al. NitroSynapsin therapy for a mouse MEF2C haploinsufficiency model of human autism. *Nat. Commun.* **8**, 1488 (2017).
 34. Parikshak, N. N. et al. Integrative functional genomic analyses implicate specific molecular pathways and circuits in autism. *Cell* **155**, 1008–1021 (2013).
 35. Li, H. et al. Transcription factor MEF2C influences neural stem/progenitor cell differentiation and maturation in vivo. *Proc. Natl. Acad. Sci. USA* **105**, 9397–9402 (2008).
 36. Chahrour, M. et al. MeCP2, a key contributor to neurological disease, activates and represses transcription. *Science* **320**, 1224–1229 (2008).
 37. Wang, Y. M. et al. MicroRNA-197 controls ADAM10 expression to mediate MeCP2's role in the differentiation of neuronal progenitors. *Cell Death Differ.* **26**, 1863–1879 (2019).
 38. Chaudhary, R., Agarwal, V., Kaushik, A. S. & Rehman, M. Involvement of myocyte enhancer factor 2c in the pathogenesis of autism spectrum disorder. *Heliyon* **7**, e06854 (2021).
 39. Zweier, M. et al. Mutations in MEF2C from the 5q14.3q15 microdeletion syndrome region are a frequent cause of severe mental retardation and diminish MECP2 and CDKL5 expression. *Hum. Mutat.* **31**, 722–733 (2010).
 40. Edmondson, D. G., Lyons, G. E., Martin, J. F. & Olson, E. N. Mef2 gene expression marks the cardiac and skeletal muscle lineages during mouse embryogenesis. *Development* **120**, 1251–1263 (1994).
 41. Zhang, Z. & Zhao, Y. Progress on the roles of MEF2C in neuropsychiatric diseases. *Mol. Brain* **15**, 8 (2022).
 42. Le Meur, N. et al. MEF2C haploinsufficiency caused by either microdeletion of the 5q14.3 region or mutation is responsible for severe mental retardation with stereotypic movements, epilepsy and/or cerebral malformations. *J. Med. Genet.* **47**, 22–29 (2010).
 43. Novara, F. et al. Refining the phenotype associated with MEF2C haploinsufficiency. *Clin. Genet.* **78**, 471–477 (2010).
 44. Nowakowska, B. A. et al. Severe mental retardation, seizures, and hypotonia due to deletions of MEF2C. *Am. J. Med. Genet. B Neuropsychiatr. Genet.* **153b**, 1042–1051 (2010).
 45. Paciorkowski, A. R. et al. MEF2C Haploinsufficiency features consistent hyperkinesia, variable epilepsy, and has a role in dorsal and ventral neuronal developmental pathways. *Neurogenetics* **14**, 99–111 (2013).
 46. Engels, H. et al. A novel microdeletion syndrome involving 5q14.3-q15: clinical and molecular cytogenetic characterization of three patients. *Eur. J. Hum. Genet.* **17**, 1592–1599 (2009).
 47. Novara, F. et al. MEF2C deletions and mutations versus duplications: a clinical comparison. *Eur. J. Med. Genet.* **56**, 260–265 (2013).
 48. Cesaretti, C. et al. Prenatal detection of 5q14.3 duplication including MEF2C and brain phenotype. *Am. J. Med. Genet. A* **170a**, 1352–1357 (2016).
 49. Shadrin, A. A. et al. Novel loci associated with attention-deficit/hyperactivity disorder are revealed by leveraging polygenic overlap

- with educational attainment. *J. Am. Acad. Child Adolesc. Psychiatry* **57**, 86–95 (2018).
50. Cooley Coleman, J. A. et al. Comprehensive investigation of the phenotype of MEF2C-related disorders in human patients: A systematic review. *Am. J. Med. Genet. A* **185**, 3884–3894 (2021).
 51. Deciphering Developmental Disorders Study. Prevalence and architecture of de novo mutations in developmental disorders. *Nature* **542**, 433–438 (2017).
 52. Sanders, S. J. et al. Insights into autism spectrum disorder genomic architecture and biology from 71 risk loci. *Neuron* **87**, 1215–1233 (2015).
 53. Schaufele, F. et al. The structural basis of androgen receptor activation: intramolecular and intermolecular amino-carboxy interactions. *Proc. Natl. Acad. Sci. USA* **102**, 9802–9807 (2005).
 54. van Royen, M. E., van Cappellen, W. A., de Vos, C., Houtsmuller, A. B. & Trapman, J. Stepwise androgen receptor dimerization. *J. Cell Sci.* **125**, 1970–1979 (2012).
 55. Amir, R. E. et al. Rett syndrome is caused by mutations in X-linked MECP2, encoding methyl-CpG-binding protein 2. *Nat. Genet.* **23**, 185–188 (1999).
 56. Fisher, C. R., Graves, K. H., Parlow, A. F. & Simpson, E. R. Characterization of mice deficient in aromatase (ArKO) because of targeted disruption of the cyp19 gene. *Proc. Natl. Acad. Sci. USA* **95**, 6965–6970 (1998).
 57. Jones, M. E. et al. Aromatase-deficient (ArKO) mice have a phenotype of increased adiposity. *Proc. Natl. Acad. Sci. USA* **97**, 12735–12740 (2000).
 58. Tsuda, M. C., Nagata, K., Sagoshi, S. & Ogawa, S. Estrogen and oxytocin involvement in social preference in male mice: a study using a novel long-term social preference paradigm with aromatase, estrogen receptor- α and estrogen receptor- β , oxytocin, and oxytocin receptor knockout male mice. *Integr. Zool.* **13**, 698–710 (2018).
 59. Hu, V. W., Sarachana, T., Sherrard, R. M. & Kocher, K. M. Investigation of sex differences in the expression of RORA and its transcriptional targets in the brain as a potential contributor to the sex bias in autism. *Mol. Autism* **6**, 7 (2015).
 60. Courchesne, E., Campbell, K. & Solso, S. Brain growth across the life span in autism: age-specific changes in anatomical pathology. *Brain Res.* **1380**, 138–145 (2011).
 61. Redcay, E. & Courchesne, E. When is the brain enlarged in autism? A meta-analysis of all brain size reports. *Biol. Psychiatry* **58**, 1–9 (2005).
 62. Courchesne, E., Carper, R. & Akshoomoff, N. Evidence of brain overgrowth in the first year of life in autism. *Jama* **290**, 337–344 (2003).
 63. Dawson, G. et al. Rate of head growth decelerates and symptoms worsen in the second year of life in autism. *Biol. Psychiatry* **61**, 458–464 (2007).
 64. Hazlett, H. C. et al. Early brain development in infants at high risk for autism spectrum disorder. *Nature* **542**, 348–351 (2017).
 65. Cheng, T. L. et al. MeCP2 suppresses nuclear microRNA processing and dendritic growth by regulating the DGCR8/Drosha complex. *Dev. Cell* **28**, 547–560 (2014).
 66. Telley, L. et al. Temporal patterning of apical progenitors and their daughter neurons in the developing neocortex. *Science* **364**, eaav2522 (2019).

Acknowledgements

We thank all members of Zheng's laboratory for their support. The research was supported by funds from the National Key R&D Program of China 2024YFA1306000 to Yufang Zheng; the Natural Science Foundation of Shanghai 24ZR1449600 to Yu-Meng Wang; the National Natural Science Foundation of China 32370861 and 32170814 to Yufang Zheng, 81901159 to Yu-Meng Wang, and 82101218 to Yanyan Jia.

Author contributions

Y.Z. and Y.-M.W. conceived the project. Y.Z. supervised the project and provided guidance throughout. Y.-M.W. designed the experiments and performed all the experiments with the assistances from Y.J., Y.W. and Q. Z. Y.-M.W., Y.Z., Y.J. and Y.W. analyzed the data and wrote the manuscript. Y.Z., Y.-M.W., Y.J., Y.G., L.Z. and M.J. reviewed and edited the manuscript. All authors discussed the results and commented on the manuscript.

Competing interests

The authors declare no competing interests.

Additional information

Supplementary information The online version contains supplementary material available at <https://doi.org/10.1038/s41467-026-72942-3>.

Correspondence and requests for materials should be addressed to Yu-Meng Wang, Li Zhang, Min Jin or Yufang Zheng.

Peer review information *Nature Communications* thanks Alex Tsompanidis and Rong Zhang for their contribution to the peer review of this work. A peer review file is available.

Reprints and permissions information is available at <http://www.nature.com/reprints>

Publisher's note Springer Nature remains neutral with regard to jurisdictional claims in published maps and institutional affiliations.

Open Access This article is licensed under a Creative Commons Attribution-NonCommercial-NoDerivatives 4.0 International License, which permits any non-commercial use, sharing, distribution and reproduction in any medium or format, as long as you give appropriate credit to the original author(s) and the source, provide a link to the Creative Commons licence, and indicate if you modified the licensed material. You do not have permission under this licence to share adapted material derived from this article or parts of it. The images or other third party material in this article are included in the article's Creative Commons licence, unless indicated otherwise in a credit line to the material. If material is not included in the article's Creative Commons licence and your intended use is not permitted by statutory regulation or exceeds the permitted use, you will need to obtain permission directly from the copyright holder. To view a copy of this licence, visit <http://creativecommons.org/licenses/by-nc-nd/4.0/>.

© The Author(s) 2026